The Astrophysical Journal, 818:116 (20pp), 2016 February 20 doi:10.3847/0004-637X/818/2/116

THE GOULD'S BELT VERY LARGE ARRAY SURVEY. V. THE PERSEUS REGION

Gerardo Pech[1], Laurent Loinard[1,2], Sergio A. Dzib[2], Amy J. Mioduszewski[3], Luis F. Rodríguez[1,4], Gisela N. Ortiz-León[1], Juana L. Rivera[1], Rosa M. Torres[5], Andrew F. Boden[6], Lee Hartman[7], Marina A. Kounkel[7], Neal J. Evans II[8], Cesar Briceño[9], John Tobin[10], and Luis A. Zapata[1]

[1] Instituto de Radioastronomía y Astrofísica, Universidad Nacional Autónoma de México, Apartado Postal 3-72, 58089 Morelia, Michoacán, México; g.pech@crya.unam.mx
[2] Max-Planck-Institut für Radioastronomie, Auf dem Hügel 69, D-53121 Bonn, Germany
[3] National Radio Astronomy Observatory, Domenici Science Operations Center, 1003 Lopezville Road, Socorro, NM 87801, USA
[4] King Abdulaziz University, P.O. Box 80203, Jeddah 21589, Saudi Arabia
[5] Centro Universitario de Tonalá, Universidad de Guadalajara, Avenida Nuevo Periférico No. 555, Ejido San José Tatepozco, C.P. 48525, Tonalá, Jalisco, Mexico
[6] Division of Physics, Math and Astronomy, California Institute of Technology, 1200 East California Boulevard, Pasadena, CA 91125, USA
[7] Department of Astronomy, University of Michigan, 500 Church Street, Ann Arbor, MI 48105, USA
[8] Department of Astronomy, The University of Texas at Austin, 1 University Station, C1400, Austin, TX 78712, USA
[9] Cerro Tololo Inter-American Observatory, Casilla 603, La Serena, Chile
[10] Leiden Observatory, Leiden University, P.O. Box 9513, 2300 RA Leiden, The Netherlands
Received 2015 July 15; accepted 2015 November 23; published 2016 February 12

ABSTRACT

We present multiepoch, large-scale (~2000 arcmin^2), fairly deep (~16 μJy), high-resolution (~1″) radio observations of the Perseus star-forming complex obtained with the Karl G. Jansky Very Large Array at frequencies of 4.5 and 7.5 GHz. These observations were mainly focused on the clouds NGC 1333 and IC 348, although we also observed several fields in other parts of the Perseus complex. We detect a total of 206 sources, 42 of which are associated with young stellar objects (YSOs). The radio properties of about 60% of the YSOs are compatible with a nonthermal radio emission origin. Based on our sample, we find a fairly clear relation between the prevalence of nonthermal radio emission and evolutionary status of the YSOs. By comparing our results with previously reported X-ray observations, we show that YSOs in Perseus follow a Güdel–Benz relation with $\kappa = 0.03$, consistent with other regions of star formation. We argue that most of the sources detected in our observations but not associated with known YSOs are extragalactic, but provide a list of 20 unidentified radio sources whose radio properties are consistent with being YSO candidates. Finally, we also detect five sources with extended emission features that can clearly be associated with radio galaxies.

Key words: radiation mechanisms: nonthermal – radiation mechanisms: thermal – radio continuum: stars – techniques: interferometric

1. INTRODUCTION

The Perseus molecular complex is part of the ring-like structure of molecular clouds known as Gould's Belt. It is of particular interest because it contains several of the regions within about 300 pc of the Sun that are most actively forming low- and intermediate-mass stars (Bally et al. 2008, p. 308). In this paper we describe the results of deep, large-scale radio observations of the Perseus complex, particularly of NGC 1333 and IC 348. NGC 1333 is currently the most active region of star formation in the Perseus molecular cloud (see Walawender et al. 2008, p. 346 for a recent review). It is one of the best-studied extremely young clusters of low- to intermediate-mass stars, and one of the most active sites of ongoing star formation within 500 pc of the Sun. The molecular mass contained in the NGC 1333 region is approximately 450 $M_\odot$ (Warin et al. 1996). The cluster contains about 150 young stars with a median age of about 10^6 yr and a total mass in stars of about 100 $M_\odot$ (Walawender et al. 2008, p. 346). Distance determinations locate NGC 1333 at aproximately 235 pc (Hirota et al. 2008). The IC 348 region, on the other hand, is particularly important because it is well surveyed at a variety of wavelengths and intermediate in nature between dense clusters and loose associations (see Herbst 2008, p. 372 for a recent review). It contains at least 360 stellar members, with a median age of ~2–3 Myr, but this number may be as high as ~400 (Muench et al. 2007) and with total mass in stars of about 80 $M_\odot$. It contains at least 26 brown dwarfs, as well as some protostars, Herbig–Haro objects, and starless submillimeter cores. Distance measurements to IC 348 agree on a value of 300 pc (Herbst 2008, p. 372). This would place NGC 1333 and IC 348 at somewhat different distances.

Different mechanisms are required to explain the radio emission of young stars. These are either thermal (bremsstrahlung from H II regions or shocks/jets, winds, accretion flows, etc.) or nonthermal (gyrosynchrotron radiation from flares). Embedded Class I protostars are known to drive collimated thermal winds or jets, so they are usually detected as thermal bremsstrahlung sources. For more massive stars, the radio emission can also originate from optically thick or thin compact H II regions (Hughes 1988; Estalella et al. 1991; Gómez et al. 2000). More evolved young stellar objects (YSOs) (Class III sources) often exhibit nonthermal emission, but this type of emission has also been detected in some Class II and Class I sources (Forbrich et al. 2007; Dzib et al. 2010; Deller et al. 2013). This emission is typically believed to arise from gyrosynchroton radiation from mildly relativistic electrons gyrating in the magnetosphere of YSOs. Gyrosynchrotron emission is characterized by a high brightness temperature, usually a high level of variability, and often a negative spectral index and some level of circular polarization (Hughes 1991; Hughes et al. 1995; Garay et al. 1996).

In this paper we present observations obtained with the Karl G. Jansky Very Large Array (VLA) of the Perseus molecluar

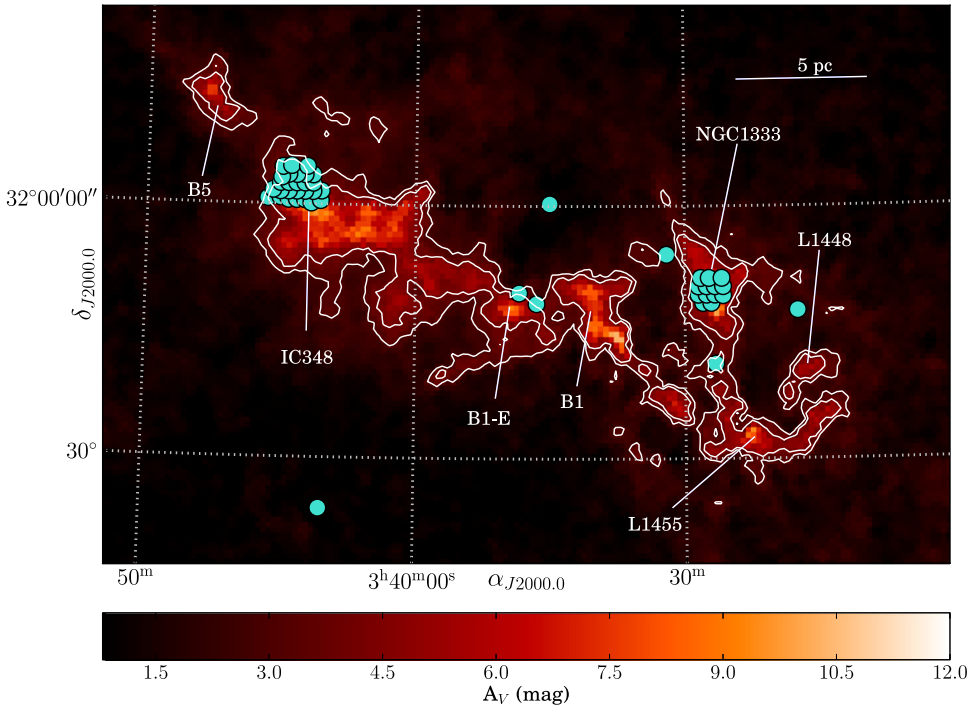

Figure 1. Extinction map of the Perseus complex obtained as part of the COMPLETE project (Ridge et al. 2006) based on the 2MASS data (Skrutskie et al. 2006). A linear distance is provided (assuming a distance of 235 pc to the entire region; Hirota et al. 2008). The turquoise circles indicate the areas mapped with the VLA for the survey presented here. The diameter of each circle is 6′ and corresponds to the primary beam of the VLA at 7.5 GHz. Note that the field of view, and therefore also the total mapped area, at 4.5 GHz is significantly larger.

cloud and continue the work by Dzib et al. (2013, 2015), Kounkel et al. (2014), and Ortiz-León et al. (2015) to discuss the population of radio sources in star-forming regions contained within Gould's Belt and identify adequate target candidates for very long baseline interferometry (VLBI) observations as part of the Gould's Belt Distance Survey (Loinard et al. 2011). This survey is aimed at measuring the distance to about 200 young stars distributed across five regions in Gould's Belt (Ophiuchus, Taurus, Perseus, Serpens, and Orion).

2. OBSERVATIONS

The observations were collected with the VLA of the National Radio Astronomy Observatory in B and BnA configurations. Two frequency subbands, each 1 GHz wide and centered at 4.5 and 7.5 GHz, respectively, were recorded simultaneously. The observations were obtained in three sessions, on 2011 March 06/13, April 14/25, and May 01/02/10/19/22, typically separated from one another by a month. This dual-frequency, multiepoch strategy was chosen to enable the characterization of the spectral index and variability of the detected sources, as well as to help with the identification of the emission mechanisms.

Our observations cover mainly the NGC 1333 and IC 348 star-forming regions (see Figure 1). We mapped the NGC 1333 area using a mosaic of 13 VLA pointings and the IC 348 area using a mosaic of 27 VLA pointings. Additionally, seven pointings were selected to cover regions associated with other dust clouds. The distribution of the individual pointings in NGC 1333 and IC 348 follows a somewhat irregular pattern chosen to optimize the compromise between uniform sensitivity and the inclusion of the largest possible number of known young stars (see Figure 1). The FWHM of the primary beam (i.e., the field of view) of the VLA has a diameter of 10′ at 4.5 GHz and 6′ at 7.5 GHz. As a consequence, and taking into account the overlap of the beams, the mosaic of NGC 1333 covers an area of ∼432 arcmin^2 at 4.5 GHz and ∼235 arcmin^2 at 7.5 GHz. The area covered by the IC 348 mosaic is ∼800 arcmin^2 at 4.5 GHz and ∼475 arcmin^2 at 7.5 GHz. All the observing sessions were organized as follows. The standard flux calibrator 3C 147 was first observed for ∼10 minutes. We subsequently spent 1 minute on the phase calibrator J0336 +3218, followed by a series of three target pointings, spending 3 minutes on each. This phase calibrator/target sequence was repeated until all target fields were observed. Thus, 3 minutes were spent on each target field for each epoch.

All data sets were edited and calibrated in a standard fashion using the Common Astronomy Software Applications package (CASA). Once calibrated, the data at each frequency were imaged (Stokes parameter *I*) using the CASA task `clean`. The NGC 1333 and IC 348 mosaics were constructed by setting the *imagermode* parameter to "mosaic" in the `clean` task. In order to take into account the non-coplanarity of the baselines far from the phase center, we set the *gridmode* parameter to "widefield" with *wprojplanes* = 64. We also corrected the images for the primary beam attenuation. The *weighting* parameter in `clean` was set to "briggs" with *robust* subparameter set to 0.0. For wide fields of view (such as those considered here), bandwidth smearing can become an issue, causing the peak flux of a point source to be reduced while conserving its integrated flux density. This worsens for sources at large distances from the phase center. To avoid this effect, all our observations were imaged using a multifrequency scale (`mode = ''mfs''` in `clean`). This algorithm projects different frequencies onto different points of the uv-plane (Rau & Cornwell 2011).

Table 1
VLA Observations

Region	Epoch[a]	Synthesized Beam[b] ($\theta_{maj} \times \theta_{min}$; P.A.)		rms Noise[c] (μJy beam^{-1})	
		4.5 GHz	7.5 GHz	4.5 GHz	7.5 GHz
NGC 1333	1	1.″29 × 1.″00, 97.7	0.″80 × 0.″61, 99.4	26	23
	2	2.″43 × 0.″94, 75.7	1.″52 × 0.″58, 74.6	35	30
	3	2.″26 × 0.″81, 63.5	1.″32 × 0.″64, 65.9	38	31
	C	1.″40 × 0.″90, 65.0	0.″90 × 0.″50, 66.0	16	18
IC 348	1	1.″10 × 1.″01, −24.5	0.″68 × 0.″61, −23.0	18	18
	2	1.″59 × 1.″02, 85.6	1.″00 × 0.″64, 62.6	21	25
	3	1.″41 × 0.″37, 62.7	0.″92 × 0.″23, 62.6	33	27
	C	1.″17 × 0.″63, 65.6	0.″79 × 0.″34, 62.6	16	15
Singles[d]	1	1.″37 × 1.″06, 98.7	0.″84 × 0.″64, 98.9	35	37
	2	1.″64 × 0.″35, 90.9	0.″99 × 0.″22, 100.17	47	50
	3	1.″11 × 0.″63, 65.6	0.″79 × 0.″34, −37.0	51	48
	C	1.3.″ ×0.″54, 99.0	0.″82 × 0.″32, −79.5	29	28

Notes.
[a] C indicates parameters measured in the images after combining the epochs.
[b] Units are arcseconds and degrees, respectively.
[c] Measured at the center of the Stokes *I* image.
[d] Average values in the seven individual fields.

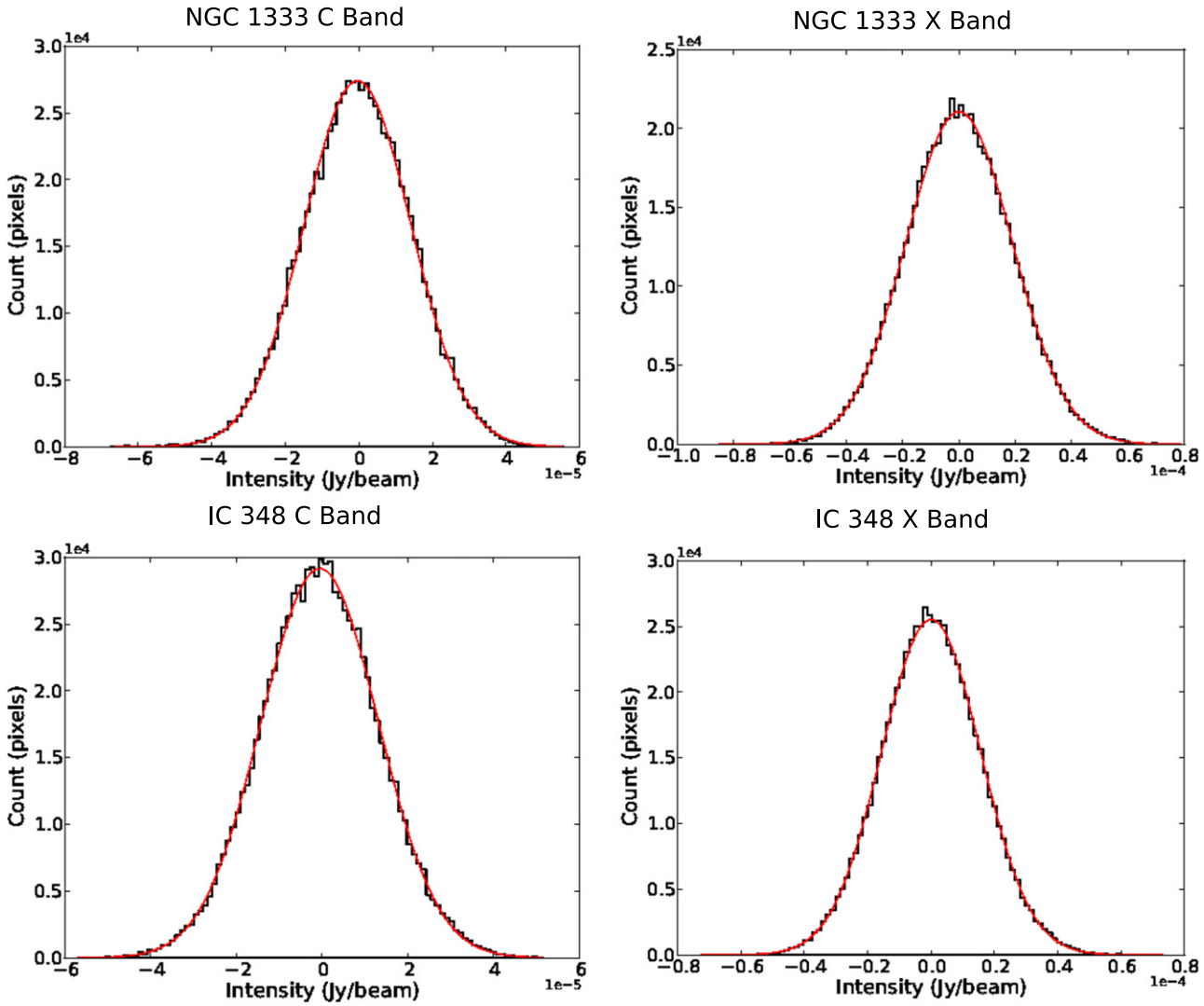

Figure 2. Histograms of the pixel values of the noise in radio maps of NGC 1333 and IC 348 at 4.5 and 7.5 GHz. The red line is a Gaussian fit to its respective histrogram.

Table 2
Radio Sources Detected in NGC 1333

GBS-VLA Name	New Source[a]	Flux Properties				Spectral Index
		$f_{4.5}$(mJy)	Var.$_{4.5}$ (%)	$f_{7.5}$(mJy)	Var.$_{7.5}$ (%)	
J032813.80+311755.1	Y	0.10 ± 0.02	>69 ± 11	…	…	…
J032819.46+311831.0	Y	0.65 ± 0.10	36 ± 15	0.19 ± 0.06	>23 ± 34	−2.5 ± 0.3
J032820.31+312509.4	Y	0.15 ± 0.03	31 ± 32	0.05 ± 0.03	>16 ± 46	−2.0 ± 0.7
J032821.37+311440.1	N	0.37 ± 0.06	35 ± 18	…	…	…
J032821.70+311555.0	Y	0.07 ± 0.02	>26 ± 28	<0.06	…	<−0.4 ± 0.5
J032822.25+311427.1	N	0.43 ± 0.07	33 ± 19	…	…	…
J032825.98+311616.0	Y	0.34 ± 0.04	52 ± 11	0.08 ± 0.02	>18 ± 35	−3.0 ± 0.5
J032826.24+312440.6	Y	0.07 ± 0.02	52 ± 34	<0.07	…	<−0.1 ± 0.5
J032832.21+313012.7	Y	0.08 ± 0.02	>45 ± 19	…	…	…
J032832.41+311245.3	Y	0.12 ± 0.03	> 4 ± 33	…	…	…
J032832.87+311445.3	N	1.10 ± 0.12	16 ± 14	0.59 ± 0.14	31 ± 25	−1.3 ± 0.2
J032833.25+313043.5	Y	0.09 ± 0.02	>64 ± 21	…	…	…
J032837.01+312125.3	N	0.43 ± 0.03	21 ± 10	0.35 ± 0.03	30 ± 12	−0.4 ± 0.2
J032837.10+311330.7	N	0.10 ± 0.02	>25 ± 24	…	…	…
J032843.65+311702.7	N	0.08 ± 0.02	> 8 ± 43	…	…	…
J032846.49+312943.5	Y	0.46 ± 0.10	>87 ± 4	…	…	…
J032849.45+312841.7	N	1.50 ± 0.22	14 ± 18	0.90 ± 0.29	56 ± 20	−1.0 ± 0.2
J032850.72+312225.2	N	1.40 ± 0.09	17 ± 8	1.27 ± 0.11	5 ± 14	−0.2 ± 0.2
J032851.99+310924.6	Y	0.09 ± 0.03	>36 ± 23	…	…	…
J032856.92+311622.2	N	0.10 ± 0.02	>38 ± 15	0.12 ± 0.03	–A–	0.5 ± 0.6
J032857.30+311531.4	N	0.06 ± 0.02	>72 ± 9	…	…	…
J032857.36+311415.8	N	0.15 ± 0.02	15 ± 27	0.18 ± 0.03	20 ± 23	0.3 ± 0.3
J032857.37+312954.0	Y	0.09 ± 0.02	35 ± 46	…	…	…
J032857.40+312953.9	Y	0.10 ± 0.02	>36 ± 36	…	…	…
J032857.65+311531.4	N	0.56 ± 0.05	23 ± 10	0.33 ± 0.05	39 ± 19	−1.1 ± 0.2
J032859.25+312033.0	N	0.12 ± 0.02	43 ± 22	0.12 ± 0.03	42 ± 26	0.1 ± 0.5
J032859.27+311548.2	N	0.11 ± 0.02	>84 ± 2	0.09 ± 0.02	>70 ± 9	−0.5 ± 0.5
J032859.66+312542.7	N	0.12 ± 0.02	35 ± 24	…	…	…
J032859.83+311402.8	N	0.16 ± 0.02	24 ± 19	0.13 ± 0.02	>43 ± 11	−0.4 ± 0.4
J032900.23+313029.7	Y	0.09 ± 0.03	>40 ± 29	…	…	…
J032900.30+312957.6	Y	0.07 ± 0.02	>33 ± 19	…	…	…
J032900.37+312045.4	N	0.08 ± 0.02	>50 ± 10	0.05 ± 0.02	> 6 ± 31	−1.0 ± 0.9
J032901.21+312026.0	N	0.12 ± 0.02	34 ± 28	0.09 ± 0.03	–A–	−0.5 ± 0.6
J032901.63+312018.6	N	0.11 ± 0.02	28 ± 26	0.08 ± 0.03	>14 ± 37	−0.6 ± 0.6
J032901.96+311538.0	N	1.03 ± 0.08	5 ± 12	1.08 ± 0.15	22 ± 17	0.1 ± 0.2
J032902.43+312924.6	Y	0.07 ± 0.02	>32 ± 26	…	…	…
J032903.14+312752.6	Y	0.11 ± 0.02	17 ± 39	<0.06	…	<−1.4 ± 0.3
J032903.38+311601.6	N	0.08 ± 0.02	>51 ± 15	0.05 ± 0.02	>36 ± 28	−0.8 ± 0.8
J032903.75+311603.7	N	0.10 ± 0.02	69 ± 19	0.21 ± 0.04	35 ± 28	1.5 ± 0.4
J032904.06+311446.2	N	0.07 ± 0.02	–A–	<0.05	>52 ± 24	<−0.5 ± 0.5
J032904.26+311609.0	N	0.12 ± 0.02	63 ± 17	0.07 ± 0.02	24 ± 68	−1.0 ± 0.6
J032907.13+312635.2	Y	0.14 ± 0.02	44 ± 21	0.10 ± 0.02	15 ± 32	−0.6 ± 0.5
J032907.16+311708.9	N	0.09 ± 0.02	19 ± 30	<0.06	…	<−0.9 ± 0.4
J032907.75+312157.1	N	0.08 ± 0.02	>28 ± 20	0.19 ± 0.03	35 ± 25	1.7 ± 0.5
J032907.87+312348.0	Y	0.10 ± 0.02	>57 ± 13	0.05 ± 0.02	>37 ± 29	−1.4 ± 1.0
J032909.14+312144.0	N	0.11 ± 0.02	>67 ± 7	0.15 ± 0.03	>68 ± 14	0.6 ± 0.5
J032909.64+311450.5	Y	0.09 ± 0.02	>39 ± 36	0.07 ± 0.02	>49 ± 32	−0.4 ± 0.7
J032910.22+312335.1	N	0.05 ± 0.02	>18 ± 30	<0.06	…	< 0.3 ± 0.7
J032910.39+312159.0	N	0.48 ± 0.03	16 ± 12	0.35 ± 0.03	7 ± 23	−0.6 ± 0.2
J032910.42+311332.0	N	0.05 ± 0.02	>17 ± 31	0.14 ± 0.03	>38 ± 33	2.1 ± 0.7
J032910.53+311330.9	N	0.07 ± 0.02	> 4 ± 29	0.11 ± 0.03	>36 ± 20	1.0 ± 0.6
J032911.25+311831.1	N	0.16 ± 0.02	42 ± 13	0.19 ± 0.02	41 ± 20	0.3 ± 0.3
J032914.11+313057.5	Y	0.11 ± 0.03	>38 ± 24	…	…	…
J032915.85+311621.4	N	0.10 ± 0.02	>52 ± 13	0.11 ± 0.04	>36 ± 22	0.2 ± 0.8
J032916.59+311648.7	N	0.08 ± 0.02	>53 ± 15	0.14 ± 0.04	>61 ± 13	1.2 ± 0.6
J032917.67+312244.9	N	0.09 ± 0.02	>31 ± 19	0.13 ± 0.03	32 ± 41	0.8 ± 0.5
J032918.56+311427.3	Y	0.07 ± 0.02	76 ± 15	…	…	…
J032920.35+312108.5	Y	0.10 ± 0.02	>34 ± 29	…	…	…
J032920.67+311549.5	N	2.10 ± 0.26	Extended	0.98 ± 0.24	51 Extended	−1.5 ± 0.2
J032922.29+311354.2	N	0.30 ± 0.05	21 ± 21	0.22 ± 0.08	21 ± 43	−0.6 ± 0.3
J032923.95+311620.0	N	0.49 ± 0.05	16 ± 14	0.28 ± 0.06	9 ± 39	−1.2 ± 0.3
J032926.55+310937.0	Y	0.07 ± 0.02	>58 ± 24	…	…	…
J032926.57+312254.5	Y	0.05 ± 0.02	>55 ± 28	…	…	…

Table 2
(Continued)

GBS-VLA Name	New Source[a]	Flux Properties				Spectral Index
		$f_{4.5}$(mJy)	Var.$_{4.5}$ (%)	$f_{7.5}$(mJy)	Var.$_{7.5}$ (%)	
J032927.38+312255.2	Y	0.04 ± 0.02	>15 ± 28	⋯	⋯	⋯
J032929.04+312802.4	Y	0.08 ± 0.02	49 ± 28	<0.06	>11 ± 34	<−0.5 ± 0.5
J032930.94+312211.8	N	0.85 ± 0.05	16 ± 9	0.76 ± 0.05	4 ± 15	−0.2 ± 0.2
J032931.95+312121.9	N	0.06 ± 0.02	>29 ± 24	⋯	⋯	⋯
J032933.19+312845.2	Y	0.07 ± 0.02	>71 ± 24	<0.07	⋯	<−0.2 ± 0.5
J032933.78+311800.8	Y	0.05 ± 0.02	>44 ± 28	⋯	⋯	⋯
J032936.98+311701.9	Y	0.09 ± 0.02	>47 ± 27	0.06 ± 0.02	>28 ± 39	−0.9 ± 0.8
J032939.39+312309.2	Y	0.14 ± 0.04	>47 ± 27	<0.06	⋯	<−1.9 ± 0.6
J032944.99+312019.7	Y	0.15 ± 0.03	>58 ± 18	<0.06	⋯	<−1.8 ± 0.4
J032946.15+312353.7	Y	0.06 ± 0.02	>27 ± 30	⋯	⋯	⋯
J032950.32+312646.5	Y	0.08 ± 0.03	>51 ± 27	⋯	⋯	⋯

Notes. The A annotation indicates a source not detected at three times the noise level on individual epochs, but detected on the image of the concatenated epochs.
[a] Y—source without reported counterparts at any frequency. N—source with known counterpart.

The noise levels in NGC 1333 and IC 348 were uniform across the mosaics and of order 20–30 μJy at both frequencies in the individual epochs (see Table 1). For the individual fields, noise levels of 35–50 μJy were reached at both frequencies in the individual epochs (see Table 1). The improved noise levels in the mosaics result from the overlap between the individual fields. To produce images with improved sensitivity, the three epochs were combined, resulting in noise levels of 15–18 μJy uniformly across the mosaics and ∼28 μJy for the individual fields (see again Table 1). The synthesized beam was order of 1″ and is given explicitly for each epoch, region, and frequency in Table 1.

3. RESULTS

To identify sources in our observations, we use the concatenation of the three epochs, which provides the highest sensitivity. Sources were first searched for using an automated source identification. The automated source identification was made using the `find sources` function in the `casaviewer`. However, automated identification resulted in some false-positive detections and failed to detect some real sources (particularly near the outer edges of the images). Therefore, a visual inspection of the mosaics was performed in order to verify or discard the sources found by the automated identification and to identify sources not detected by the automated identification. The criteria used to consider a detection as firm were (1) sources with a reported conterpart and a flux larger than three times the σ noise of the area, and (2) sources with a flux larger than five times the σ noise of the area and without reported counterparts. This procedure was adopted to minimize the possibility of reporting a large noise fluctuation as a real source.

Our source count may in principle be affected by the so-called clean bias (White et al. 1997; Condon et al. 1998). This is the effect that the `clean` algorithm can cause artificial changes to source fluxes and apparent image noise levels, i.e., it subtracts flux from real sources and redristibutes it on top of noise peaks or sidelobes. This clean bias is larger in images with poor UV-plane coverage. In order to check whether this bias affected our results, we constructed histograms of pixel values in the source-free regions of the mosaic maps of NGC 1333 and IC 348. These histograms are shown in Figure 2. We can see in these figures that the noise in our radio maps is well fitted by a Gaussian (normal) distribution, with no evidence for superimposed excesses (wings or bumps). The fact that the noise follows a normal distribution suggests that any bias that may exist in our final images is negligible. Also, given that the noise on our radio maps follows a Gaussian distribution, we can estimate the expected number of false peak detections in the maps. The probability that the value of a standard normal random variable X will exceed x is given by the complement of the standard normal cumulative distribution function $Q(x) = 1 - \phi(x)$. The cumulative distribution function, ϕ, is given by

$$\phi(x) = \frac{1}{2}\left[1 + \mathrm{erf}\left(\frac{x}{\sqrt{2}}\right)\right],$$

where erf is the error function given by

$$\mathrm{erf} = \frac{1}{\sqrt{\pi}}\int_{-x}^{x} e^{-t^2} dt.$$

With this, the probability that any independent pixel (the number of independent pixels is given by the ratio of the observed area to the area of the synthesized beam) will have a value greater than 5σ is $Q(5) \sim 3 \times 10^{-7}$. Given the number of independent pixels in our maps, we expect about 0.3 false detections in the NGC 1333 mosaic, about 1 false detection in the IC 348 mosaic, and about 1.5 false detections in the seven individual fields. Thus, we only expect about three false detections in our entire data set. This is very small compared with the number of detected sources (see below) and will have a negligible statistical effect on our interpretation of the data.

Following the procedure outlined above, a total of 206 sources were detected, 74 sources corresponding to NGC 1333, 91 sources corresponding to IC 348, and 41 sources corresponding to the seven individual fields (Tables 2–4, respectively). Only 125 of the 206 sources were detected at both frequencies; the remaining 81 were detected only in the 4.5 GHz images. To reflect the fact that these sources were found as part of the Gould's Belt VLA Survey, a source with coordinates hhmmss.ss-ddmmss.s will be named GBS-VLA Jhhmmss.ss-ddmmss.s. The fluxes of each source at 4.5 and 7.5 GHz are given in columns (3) and (5) of Tables 2–4. Three sources of uncertainties on the fluxes are included: (1) the error that results from the statistical noise in the images, (2) a

Table 3
Radio Sources Detected in IC 348

GBS-VLA Name	New Source[a]	Flux Properties				Spectral Index
		$f_{4.5}$(mJy)	Var.$_{4.5}$(%)	$f_{7.5}$(mJy)	Var.$_{7.5}$(%)	
J034311.03+320226.4	Y	0.13 ± 0.03	61 ± 22	⋯	⋯	⋯
J034313.02+320242.3	Y	0.08 ± 0.02	>47 ± 25	⋯	⋯	⋯
J034314.84+320947.6	Y	0.11 ± 0.04	>38 ± 27	⋯	⋯	⋯
J034327.28+320028.1	Y	0.14 ± 0.02	>28 ± 17	0.13 ± 0.03	>43 ± 16	−0.2 ± 0.4
J034330.40+320758.4	Y	0.22 ± 0.02	41 ± 14	⋯	⋯	⋯
J034331.68+321451.9	N	6.19 ± 1.08	21 ± 20	⋯	⋯	⋯
J034333.93+321307.4	Y	10.98 ± 1.90	33 ± 16	⋯	⋯	⋯
J034334.66+320721.1	Y	0.13 ± 0.03	8 ± 68	<0.05	⋯	<−2.0 ± 0.4
J034337.86+320649.2	N	0.05 ± 0.02	>60 ± 21	<0.05	⋯	<−0.3 ± 0.6
J034341.27+315754.1	N	0.07 ± 0.02	>47 ± 25	⋯	⋯	⋯
J034342.10+320225.2	Y	0.12 ± 0.02	>40 ± 13	⋯	⋯	⋯
J034346.30+321039.7	Y	0.33 ± 0.03	17 ± 16	0.14 ± 0.02	>49 ± 11	−1.8 ± 0.3
J034346.85+321814.8	Y	0.35 ± 0.06	41 ± 16	⋯	⋯	⋯
J034347.85+320555.2	Y	0.08 ± 0.02	>63 ± 21	⋯	⋯	⋯
J034347.95+315743.6	Y	0.09 ± 0.03	>27 ± 13	⋯	⋯	⋯
J034351.23+321309.1	N	0.12 ± 0.02	51 ± 13	0.08 ± 0.02	>49 ± 19	−0.8 ± 0.5
J034355.23+320057.2	Y	0.10 ± 0.04	>48 ± 12	⋯	⋯	⋯
J034355.41+321008.7	N	0.07 ± 0.02	>46 ± 21	⋯	⋯	⋯
J034355.52+320924.4	Y	0.06 ± 0.02	>55 ± 20	⋯	⋯	⋯
J034356.01+320928.4	N	0.21 ± 0.03	27 ± 26	0.11 ± 0.02	66 ± 28	−1.4 ± 0.4
J034356.39+321042.6	N	0.42 ± 0.04	29 ± 10	0.28 ± 0.04	13 ± 23	−0.8 ± 0.2
J034357.60+320137.3	N	0.21 ± 0.02	76 ± 6	0.17 ± 0.02	>76 ± 7	−0.4 ± 0.3
J034358.35+315754.7	Y	0.08 ± 0.02	>66 ± 21	⋯	⋯	⋯
J034359.65+320153.9	N	0.12 ± 0.02	>76 ± 4	0.14 ± 0.03	>79 ± 7	0.4 ± 0.4
J034401.19+321230.4	N	0.26 ± 0.03	25 ± 15	0.14 ± 0.03	21 ± 34	−1.3 ± 0.3
J034401.57+321232.4	Y	0.14 ± 0.02	41 ± 18	0.08 ± 0.02	>29 ± 19	−1.1 ± 0.6
J034402.03+315813.9	Y	0.07 ± 0.02	>27 ± 38	⋯	⋯	⋯
J034404.17+321526.2	Y	0.16 ± 0.02	>49 ± 9	<0.05	⋯	<−2.5 ± 0.3
J034405.59+321938.8	Y	0.15 ± 0.02	17 ± 23	0.10 ± 0.02	> 2 ± 32	−0.8 ± 0.4
J034406.38+321409.8	N	0.25 ± 0.03	25 ± 16	0.18 ± 0.02	64 ± 24	−0.6 ± 0.3
J034406.65+321236.9	N	4.56 ± 0.32	6 ± 9	3.44 ± 0.41	11 ± 15	−0.6 ± 0.1
J034408.85+320614.1	N	0.04 ± 0.02	51 ± 46	⋯	⋯	⋯
J034411.14+320314.0	N	0.04 ± 0.02	>44 ± 39	<0.05	>51 ± 42	< 0.2 ± 0.8
J034411.69+321039.4	Y	2.48 ± 0.97	Extended	0.39 ± 0.05	Extended	⋯
J034412.75+321544.4	Y	0.37 ± 0.04	26 ± 12	0.41 ± 0.07	35 ± 18	0.2 ± 0.2
J034416.02+320513.9	Y	0.18 ± 0.02	49 ± 14	⋯	⋯	⋯
J034416.17+321345.5	N	0.28 ± 0.05	47 ± 33	0.18 ± 0.03	28 ± 23	−0.8 ± 0.4
J034416.78+320956.4	N	2.89 ± 0.24	8 ± 11	1.55 ± 0.24	20 ± 18	−1.3 ± 0.1
J034420.37+320158.4	N	1.20 ± 0.10	14 ± 10	1.11 ± 0.16	7 ± 20	−0.1 ± 0.2
J034421.56+321017.4	N	0.28 ± 0.04	>89 ± 1	0.35 ± 0.06	>87 ± 6	0.4 ± 0.3
J034421.67+320624.8	N	0.08 ± 0.02	>77 ± 4	⋯	⋯	⋯
J034421.76+320918.3	N	3.99 ± 0.73	Extended	2.20 ± 1.10	Extended	⋯
J034423.11+320956.3	Y	1.54 ± 0.10	32 ± 7	0.96 ± 0.10	33 ± 10	−1.0 ± 0.2
J034424.57+320357.5	N	0.16 ± 0.03	>59 ± 17	<0.05	>80 ± 8	<−2.4 ± 0.3
J034426.15+320113.1	N	0.07 ± 0.02	53 ± 41	⋯	⋯	⋯
J034426.95+315920.0	Y	0.07 ± 0.03	84 ± 14	⋯	⋯	⋯
J034427.03+320443.5	N	0.07 ± 0.02	87 ± 8	⋯	⋯	⋯
J034431.12+320206.2	Y	0.04 ± 0.02	>51 ± 23	⋯	⋯	⋯
J034431.49+320039.6	N	0.22 ± 0.03	29 ± 22	⋯	⋯	⋯
J034431.68+321451.9	N	6.21 ± 0.45	20 ± 8	⋯	⋯	⋯
J034432.60+320842.4	N	0.39 ± 0.04	72 ± 7	0.44 ± 0.07	>88 ± 6	0.2 ± 0.2
J034432.65+321311.9	Y	3.91 ± 0.44	46 ± 10	<0.08	⋯	<−7.9 ± 0.2
J034432.77+320837.6	N	0.12 ± 0.02	30 ± 30	0.09 ± 0.03	>45 ± 33	−0.5 ± 0.6
J034432.91+321306.6	N	1.16 ± 0.15	5 ± 20	0.70 ± 0.14	>77 ± 8	−1.0 ± 0.4
J034433.04+321241.3	N	5.86 ± 0.36	Extended	4.69 ± 0.06	Extended	⋯
J034433.65+321306.4	N	3.00 ± 0.27	22 ± 10	3.04 ± 0.44	27 ± 16	0.0 ± 0.2
J034433.91+321307.5	N	12.80 ± 0.046	Extended	10.03 ± 0.99	Extended	⋯
J034434.05+320104.3	Y	0.10 ± 0.03	>82 ± 14	⋯	⋯	⋯
J034434.87+320633.5	N	0.11 ± 0.02	>42 ± 11	0.05 ± 0.02	>32 ± 39	−1.6 ± 0.7
J034435.89+320858.7	N	0.09 ± 0.02	>10 ± 24	<0.04	⋯	<−1.5 ± 0.4
J034436.47+320313.4	N	0.65 ± 0.11	56 ± 12	0.10 ± 0.02	>35 ± 23	−3.8 ± 0.4
J034436.92+320123.1	N	1.29 ± 0.12	23 ± 10	0.95 ± 0.17	25 ± 20	−0.6 ± 0.2
J034436.93+320645.4	N	0.34 ± 0.04	>75 ± 4	0.26 ± 0.06	>80 ± 8	−0.5 ± 0.3

Table 3
(Continued)

GBS-VLA Name	New Source[a]	Flux Properties				Spectral Index
		$f_{4.5}$(mJy)	Var.$_{4.5}$(%)	$f_{7.5}$(mJy)	Var.$_{7.5}$(%)	
J034437.73+321839.3	Y	0.31 ± 0.03	>76 ± 4	…	…	…
J034438.48+320820.4	Y	0.16 ± 0.02	>52 ± 9	0.09 ± 0.03	>38 ± 26	−1.1 ± 0.5
J034438.72+320841.9	N	0.18 ± 0.03	61 ± 13	0.17 ± 0.04	>61 ± 12	−0.2 ± 0.4
J034439.17+320918.4	N	0.18 ± 0.03	57 ± 11	0.19 ± 0.04	70 ± 10	0.2 ± 0.4
J034439.42+320128.8	Y	0.09 ± 0.02	>71 ± 17	…	…	…
J034443.98+320135.2	N	0.22 ± 0.02	40 ± 14	0.23 ± 0.03	33 ± 23	0.1 ± 0.3
J034446.82+320446.5	N	0.07 ± 0.02	>37 ± 25	0.06 ± 0.02	>43 ± 31	−0.5 ± 0.9
J034446.97+321455.6	N	0.93 ± 0.10	52 ± 7	0.60 ± 0.07	34 ± 11	−0.9 ± 0.2
J034447.02+321457.9	N	0.54 ± 0.06	43 ± 10	0.28 ± 0.06	>61 ± 9	−1.3 ± 0.4
J034448.89+320125.0	Y	0.12 ± 0.02	6 ± 30	0.08 ± 0.02	>43 ± 45	−1.0 ± 0.5
J034449.78+315741.7	Y	0.08 ± 0.02	>18 ± 25	…	…	…
J034450.64+321906.3	N	0.15 ± 0.02	>64 ± 9	0.14 ± 0.03	>47 ± 20	−0.2 ± 0.4
J034452.97+320507.5	N	0.47 ± 0.04	26 ± 11	0.61 ± 0.10	28 ± 18	0.5 ± 0.2
J034453.84+320436.0	N	0.33 ± 0.04	25 ± 15	0.17 ± 0.04	26 ± 28	−1.4 ± 0.3
J034458.57+320715.1	N	0.04 ± 0.02	>56 ± 24	…	…	…
J034458.67+315645.8	Y	0.06 ± 0.02	>35 ± 32	…	…	…
J034459.29+315658.9	Y	0.37 ± 0.08	46 ± 18	…	…	…
J034507.74+320027.1	N	0.06 ± 0.02	>53 ± 22	0.03 ± 0.02	>58 ± 49	−1.5 ± 1.3
J034507.97+320401.6	N	0.25 ± 0.02	37 ± 10	0.24 ± 0.03	51 ± 13	−0.1 ± 0.2
J034510.90+320822.0	N	0.36 ± 0.04	13 ± 16	0.38 ± 0.07	13 ± 25	0.1 ± 0.2
J034511.72+320219.4	Y	0.07 ± 0.02	>16 ± 28	<0.04	…	<−1.3 ± 0.5
J034513.19+321001.9	Y	0.16 ± 0.02	30 ± 20	0.07 ± 0.02	51 ± 47	−1.7 ± 0.5
J034515.99+320859.7	Y	0.29 ± 0.03	41 ± 13	0.12 ± 0.03	68 ± 26	−1.8 ± 0.3
J034516.04+320513.9	N	0.18 ± 0.02	33 ± 19	0.16 ± 0.03	51 ± 17	−0.3 ± 0.3
J034519.47+320346.8	Y	0.35 ± 0.04	19 ± 18	0.20 ± 0.05	18 ± 32	−1.1 ± 0.2
J034531.69+320400.7	Y	0.36 ± 0.03	12 ± 14	0.31 ± 0.04	25 ± 17	−0.3 ± 0.2
J034532.53+320636.9	N	1.09 ± 0.13	17 ± 14	0.56 ± 0.13	29 ± 26	−1.4 ± 0.2
J034535.64+320343.5	Y	3.13 ± 0.23	6 ± 10	1.81 ± 0.24	20 ± 15	−1.1 ± 0.2

Note.
[a] Y—source without reported counterparts at any frequency. N—source with known counterpart.

systematic uncertainty of 5% resulting from possible errors in the absolute flux calibration, and (3) uncertainties introduced by absolute pointing errors of the primary beam of the VLA antennas, as described by Dzib et al. (2014). An estimate of the radio spectral index of each source (given in column (7) of Tables 2–4) was obtained from the fluxes measured in each subband (at 4.5 and 7.5 GHz). To calculate the errors on the spectral indices, the three sources of errors on the flux at each frequency were added in quadrature, and the final error was obtained using standard error propagation theory. We are aware that this procedure to obtain errors on the spectral indices is a little conservative given that the two frequencies were recorded simultaneously, making the ratio of the two bands independent of the absolute flux uncertainty, but we prefer to maintain it to make sure we do not underestimate the errors.

Once the sources were identified in the concatenated images, we visually searched for them in the images of the individual epochs. An estimate of the level of variability of the sources was measured by comparing the fluxes measured at the three epochs. Specifically, we calculated, for each source and at each frequency, the difference between the highest and lowest measured fluxes and normalized by the maximum flux. We did not search for variability on sources with extended emission because sensitivity and UV coverage effects can produce spurious variations. The resulting values, expressed in percent, are given in columns (4) and (6) of Tables 2–4. We will consider a source as highly variable if its variability at any frequency is $\geqslant$50% at a 3σ level.

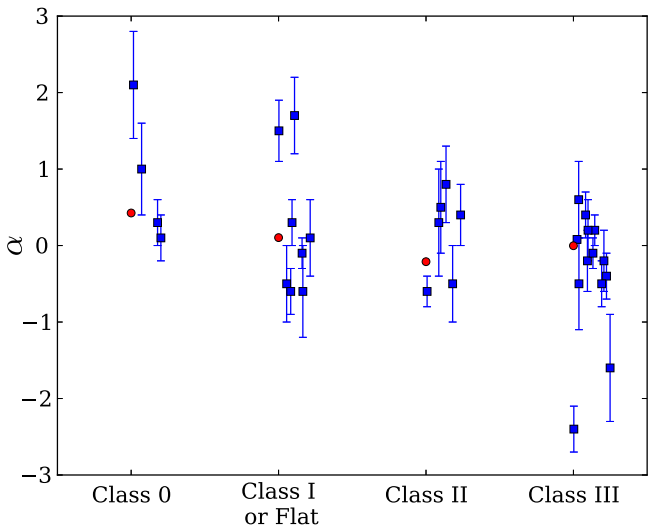

Figure 3. Spectral index as a function of the YSO evolutionary stages for YSOs in Perseus. The individual sources are shown with their error bars, and the red circles indicate the weighted average spectral index for each category.

Given the positions of the radio sources in the region mapped, the next step is to try to determine whether they are associated with a previously cataloged object and, in case they

Table 4
Radio Sources Detected in Single Fields in Perseus

GBS-VLA Name	New Source[a]	Flux Properties				Spectral Index
		$f_{4.5}$(mJy)	Var.$_{4.5}$(%)	$f_{7.5}$(mJy)	Var.$_{7.5}$(%)	
J032528.40+311109.2	N	0.33 ± 0.08	38 ± 23	···	···	···
J032549.54+311408.8	Y	0.29 ± 0.05	41 ± 21	<0.17	···	<−1.0 ± 0.3
J032827.62+304909.4	N	0.72 ± 0.21	>94 ± 2	···	···	···
J032836.79+305017.9	N	1.11 ± 0.27	23 ± 27	···	···	···
J032838.21+304007.9	N	0.42 ± 0.10	28 ± 28	···	···	···
J032840.88+304948.3	N	3.96 ± 0.86	49 ± 16	···	···	···
J032841.15+304945.2	N	3.28 ± 0.73	>92 ± 2	···	···	···
J032852.32+304216.8	N	1.60 ± 0.18	32 ± 11	1.56 ± 0.35	49 ± 17	−0.0 ± 0.2
J032855.81+304719.7	N	7.05 ± 0.70	10 ± 12	4.01 ± 0.79	22 ± 22	−1.1 ± 0.2
J032906.33+304332.7	N	0.40 ± 0.06	34 ± 18	0.42 ± 0.14	42 ± 29	0.1 ± 0.4
J032912.84+304558.5	N	0.45 ± 0.09	>65 ± 10	···	···	···
J032917.16+304329.7	N	3.30 ± 0.76	32 ± 22	···	···	···
J032919.25+304548.7	Y	0.59 ± 0.16	>96 ± 2	···	···	···
J033057.00+313402.9	Y	0.33 ± 0.08	>31 ± 19	···	···	···
J033100.54+313405.7	N	0.22 ± 0.06	>26 ± 25	···	···	···
J033100.76+313412.3	Y	0.51 ± 0.11	59 ± 15	···	···	···
J033111.09+313904.7	N	2.89 ± 0.81	44 ± 22	···	···	···
J033443.24+315912.8	Y	0.19 ± 0.04	>35 ± 26	<0.21	···	< 0.2 ± 0.3
J033454.98+320506.2	Y	0.99 ± 0.16	41 ± 14	0.79 ± 0.27	68 ± 17	−0.5 ± 0.2
J033456.97+315806.3	Y	0.15 ± 0.03	> 7 ± 28	<0.11	···	<−0.6 ± 0.4
J033501.24+320059.9	N	0.34 ± 0.03	63 ± 9	0.34 ± 0.03	>60 ± 8	0.0 ± 0.3
J033501.53+320406.0	Y	0.42 ± 0.06	4 ± 23	0.37 ± 0.10	40 ± 24	−0.3 ± 0.3
J033503.90+315923.1	Y	0.14 ± 0.03	>34 ± 16	0.20 ± 0.04	>10 ± 28	0.7 ± 0.5
J033508.31+315803.3	N	0.29 ± 0.06	49 ± 23	0.24 ± 0.08	–A–	−0.4 ± 0.5
J033509.29+315802.5	N	0.23 ± 0.05	20 ± 28	0.11 ± 0.04	–A–	−1.5 ± 0.6
J033517.06+311640.5	Y	0.50 ± 0.09	30 ± 19	0.13 ± 0.05	>28 ± 37	−2.7 ± 0.5
J033517.65+311650.0	Y	0.50 ± 0.08	50 ± 15	0.83 ± 0.56	>28 ± 38	1.0 ± 1.2
J033530.50+310955.9	Y	0.46 ± 0.07	18 ± 21	0.25 ± 0.08	>25 ± 34	−1.2 ± 0.3
J033541.20+311500.1	Y	0.57 ± 0.07	23 ± 16	0.41 ± 0.11	44 ± 24	−0.7 ± 0.2
J033542.19+311727.3	Y	0.46 ± 0.09	17 ± 26	···	···	···
J033553.36+310955.7	Y	1.46 ± 0.37	38 ± 22	···	···	···
J033620.81+311605.1	Y	0.56 ± 0.09	12 ± 21	0.57 ± 0.19	25 ± 35	0.0 ± 0.3
J033641.02+311753.1	Y	1.22 ± 0.36	51 ± 20	···	···	···
J034300.22+293317.1	N	6.63 ± 1.74	45 ± 20	···	···	···
J034300.32+293320.4	N	2.64 ± 0.70	53 ± 18	···	···	···
J034307.27+293235.0	N	1.34 ± 0.28	42 ± 17	···	···	···
J034324.29+293811.5	Y	0.43 ± 0.05	19 ± 18	0.23 ± 0.05	>36 ± 21	−1.3 ± 0.3
J034331.61+293534.5	N	1.58 ± 0.10	12 ± 9	1.38 ± 0.14	6 ± 15	−0.3 ± 0.2
J034341.43+293101.0	Y	0.46 ± 0.11	52 ± 19	···	···	···
J034344.06+294008.5	Y	0.58 ± 0.13	27 ± 24	···	···	···
J034356.20+293620.3	N	0.74 ± 0.20	46 ± 23	···	···	−−

Notes. The A annotation indicates a source not detected at three times the noise level on individual epochs, but detected on the image of the concatenated epochs.
[a] Y—source without reported counterparts at any frequency. N—source with known counterpart.

are, determine the nature of that object. We searched the literature for previous radio detections and for counterparts at X-ray, optical, near-infrared, mid-infrared, and submillimetric wavelengths. The search was done in the SIMBAD Astronomical Database and accessed all the major catalogs. We consider a radio source associated with a counterpart at another wavelength if the separation between the two was below the combined uncertainties of the two data sets. This was about 1.″5 for the optical and infrared catalog, but could be significantly larger for some of the radio catalogs. For instance, the NRAO/VLA Sky Survey (Condon et al. 1998) has a relatively lower resolution ($\theta = 45''$ FWHM), so the separation between a detection in our observations and an associated NVSS source could be as large as 15″. Additionally, this low resolution implies that one detection in the NVSS may correspond to blended emission of two or more of our detections (we will see examples of this shortly). Based on this search, we found a total of 112 sources with previously known counterparts at any frequency. Whitin these known counterparts we found 42 YSOs, 20 stars, and 8 extragalactic sources. Additionally, we found 42 objects with a known counterpart at some wavelength, but no information on the type of object. These are 25 radio sources, 12 infrared sources, 2 submillimeter sources, and 7 X-ray sources[11] (see Tables 5–7). We argue that all 25 radio sources and most (or even all) submillimeter sources, infrared sources, and X-ray sources are background objects. The remaining 94 sources are (to our knowledge) new detections not previously reported in the literature.

[11] One of these sources is both a radio and X-ray source; three of these sources are both radio and infrared sources.

Table 5
Radio Sources with Known Counterparts in NGC 1333

GBS-VLA Name	Other Names	X-Ray[a]	Infrared[b]			Radio[c]	Object Type[d]
			SST	2M	*WISE*		
J032821.37+311440.1	···	XMMU J032821.5+311440	···	···	···	···	X
J032822.25+311427.1	···	···	···	···	···	NVSS 032822+311431	Rad
J032832.87+311445.3	···	···	···	···	···	RAC97 VLA 36	E
J032837.01+312125.3	···	···	···	···	···	RAC97 VLA 37	E
J032837.10+311330.7	2MASS J03283706+3113310	···	Y	Y	Y	···	YSO
J032843.65+311702.7	···	WMW2010 19	···	···	···	···	X
J032849.45+312841.7	···	···	···	···	···	NVSS 032848+312844	Rad
J032850.72+312225.2	···	···	···	···	···	RAC97 VLA 38	YSO
J032856.92+311622.2	2MASS J032856.9+311622	···	Y	Y	Y	···	YSO
J032857.30+311531.4	···	···	···	···	···	SB86 NGC 1333 7	Rad
J032857.36+311415.8	SSTc2d J032857.4+311416	···	Y	···	···	FOW2011 8	YSO
J032857.65+311531.4	···	···	···	···	···	RAC97 VLA 1	E
J032859.25+312033.0	2MASS J03285920+312037	···	Y	Y	···	···	YSO?
J032859.27+311548.2	2MASS J03285930+3115485	CXO J032859.2+311548	Y	Y	Y	···	YSO
J032859.66+312542.7	···	WMW2010 120	···	···	···	···	X
J032859.83+311402.8	···	···	···	···	···	RAC97 VLA 12	E
J032900.37+312045.4	2MASS J03290037+3120456	CXO J032900.3+312045	Y	Y	Y	···	YSO
J032901.21+312026.0	2MASS J03290116+3120244	···	Y	Y	···	RAC97 VLA 42	YSO
J032901.63+312018.6	2MASS J03290149+3120208	···	Y	Y	Y	···	YSO
J032901.96+311538.0	HH 7–11 MMS 3	···	···	···	···	RAC97 VLA 2	YSO
J032903.38+311601.6	···	···	···	···	···	RAC97 VLA 3	YSO
J032903.75+311603.7	SVS76 NGC 1333 13A1	···	Y	Y	Y	RAC97 VLA 4a/4b	YSO
J032904.06+311446.2	SSTc2d J032904.1+311447	···	Y	Y	Y	RAC97 VLA 19	YSO
J032904.26+311609.0	2MASS J03290421+3116080	···	Y	Y	···	RAC97 VLA 20	YSO
J032907.16+311708.9	···	···	···	···	···	RAC97 VLA 23	E
J032907.75+312157.1	2MASS J03290773+3121575	WMW2010 82	Y	Y	Y	FOW2011 17	YSO
J032909.14+312144.0	2MASS J03290915+3121445	WMW2010 79	Y	Y	···	···	YSO
J032910.22+312335.1	2MASS J03291046+3123348	···	Y	Y	Y	···	YSO
J032910.39+312159.0	2MASS J03291037+3121591	CXO J032910.3+312159	Y	Y	Y	···	YSO
J032910.42+311332.0	JCC87 IRAS 4A2	···	···	···	···	···	YSO
J032910.53+311330.9	JCC87 IRAS 4A1	···	···	···	···	···	YSO
J032911.25+311831.1	SSTc2d J032911.3+311831	···	Y	···	Y	FOW2011 20	YSO
J032915.85+311621.4	···	···	···	···	···	RAC97 VLA 30	E
J032916.59+311648.7	···	···	···	···	···	RAC97 VLA 31	YSO
J032917.67+312244.9	SVS76 NGC 1333 2	CXO J032917.6+312245	Y	Y	Y	FOW2011 21	YSO
J032920.67+311549.5	···	···	···	···	···	RAC97 VLA 32	E
J032922.29+311354.2	GMM2008 38	···	···	···	···	FOW2011 25	YSO
J032923.95+311620.0	···	···	···	···	···	RAC97 VLA 35	E
J032930.94+312211.8	···	···	···	···	···	FOW2011 26	Rad
J032931.95+312121.9	···	CXO J032931.6+312125	···	···	···	···	X

Notes.
[a] XMMU—Preibisch (2003), Barcons et al. (2002); CXO—Getman et al. (2002); WMW—Winston et al. (2010).
[b] *SST*—Gutermuth et al. (2009); 2M—Cutri et al. (2003); *WISE*—Cutri et al. (2012).
[c] RAC97—Rodríguez et al. (1997), Rodríguez et al. (1999), Anglada et al. (2000); FOW2011—Forbrich et al. (2011); NVSS—Condon et al. (1998).
[d] Object type: E—extragalactic; Rad—radio source; X—X-ray source; YSO—young stellar object; YSO?—young stellar object candidate. Objects are marked as peculiar emitters (Rad, X-ray, IR or smm) when information is not sufficient to determine the nature of the object.

We searched for circular polarization (we imaged the Stokes parameter *V*) toward the detected sources located in the inner quarter (in area) of the primary beam of the VLA. Further out, beam squint can produce artificial polarization signals, so polarization measurements become unreliable. Only four souces showed a significant level of circular polarization; they are listed in Table 8.

4. DISCUSSION

4.1. YSOs and Their General Radio Properties

From all detected radio sources, 42 are associated with objects previously classified as YSOs and are listed in Table 9. Of this total, 27 objects (i.e., roughly 60%) show either high variability, a negative spectral index, or polarization, characteristics that are suggestive of nonthermal emission. Furthermore, considering that a nonthermal source with flux $\gtrsim$200 μJy can be detected in a few hours of VLBA observations, 9 of these 27 objects have a sufficient flux density to permit VLBI parallax measurements. The remaining 15 sources are not highly variable and have a spectral index that does not conclusively suggest nonthermal emission. The evolutionary status is known for 34 of the 42 YSOs detected, while 21 have a known spectral type. It has been found in other regions that, on average, more evolved stars show radio properties that resemble a nonthermal origin, i.e., they are more

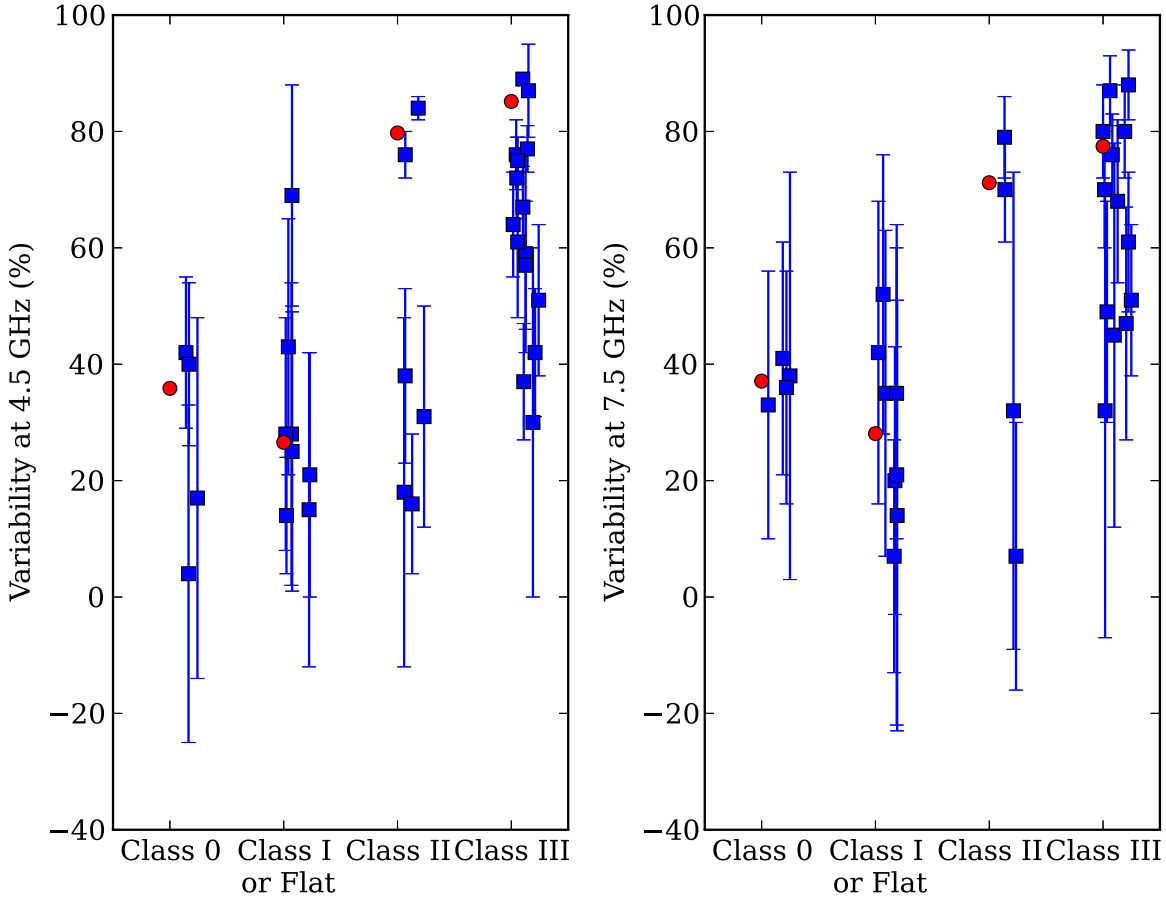

Figure 4. Variability at 4.5 GHz (left) and 7.5 GHz (right) as a function of YSO evolutionary status. The individual sources are shown with their error bars, and the red circles indicate the weighted average variability for each category.

variable and have more negative spectral indices (Dzib et al. 2013, 2015; Kounkel et al. 2014; Ortiz-León et al. 2015). In Figure 3 we plot the radio spectral index as a function of evolutionary status. On average, we can observe a tendency for more evolved YSOs to have a smaller (i.e., more negative) spectral index. This tendency is more noticeable for objects between Class 0 and Class II. The mean spectral index for Class III objects appears to divert from this tendency, but within the uncertainties, our result is in good agreement with previous ones. It indicates that the dominant emission process changes from somewhat optically thick free–free emission to either thin free–free or gyrosynchrotron emission as the YSOs evolve (see Dzib et al. 2013).

In Figure 4 we plot variability as a function of evolutionary status. There is a clear tendency for more evolved YSOs to be, on average, significantly more variable than the younger ones. This agrees with results found for other star-forming regions and is consistent with the result described above for the spectral index, as nonthermal emitters are often strongly variable. Finally, we can see in Figure 5 that in our sample, on average, the flux density does not show a clear tendency with evolutionary status; this appears to differ from previous results (see Figure 4 of Dzib et al. 2015 and Figure 5 of Dzib et al. 2013), where the radio flux appears to be higher for more evolved sources.

In Figure 6 we plot the flux density of the YSOs as a function of their spectral type (see Table 9 for references). Our detected YSOs have spectral type M, K, and G. There is only one source of type F, only one of type A, and no type B detection. We find little systematic variation of the flux with spectral type, although some M and K stars in our sample seem to have a higher-than-average flux. This would be consistent with the results reported by Dzib et al. (2015) for the Taurus region.

4.2. Background Sources

In our observations we find only eight objects that are explicitly classified as background extragalactic sources. They are all located in the NGC 1333 region and have been previously reported in VLA radio observations by Rodríguez et al. (1999), who classified them as extragalactic sources based on their negative spectral indices. We also have a large number of radio sources detected for the first time, or associated with unidentified previously reported sources at radio, IR, submillimeter, or X-ray frequencies. We argue that most of these first detections are extragalactic. Fomalont et al. (1991) showed that the number of expected background sources at 5 GHz can be described by

$$\left(\frac{N}{\mathrm{arcmin}^2}\right) = 0.42 \pm 0.05\left(\frac{S}{30\ \mu\mathrm{Jy}}\right)^{-1.18\pm0.19},$$

where N is the number of sources per arcmin^2 with flux density $>S$ (μJy). We will use this relation to examine the statistics of the sources detected. We will concentrate on the core region of each of our two mosaics (for which we have a continous

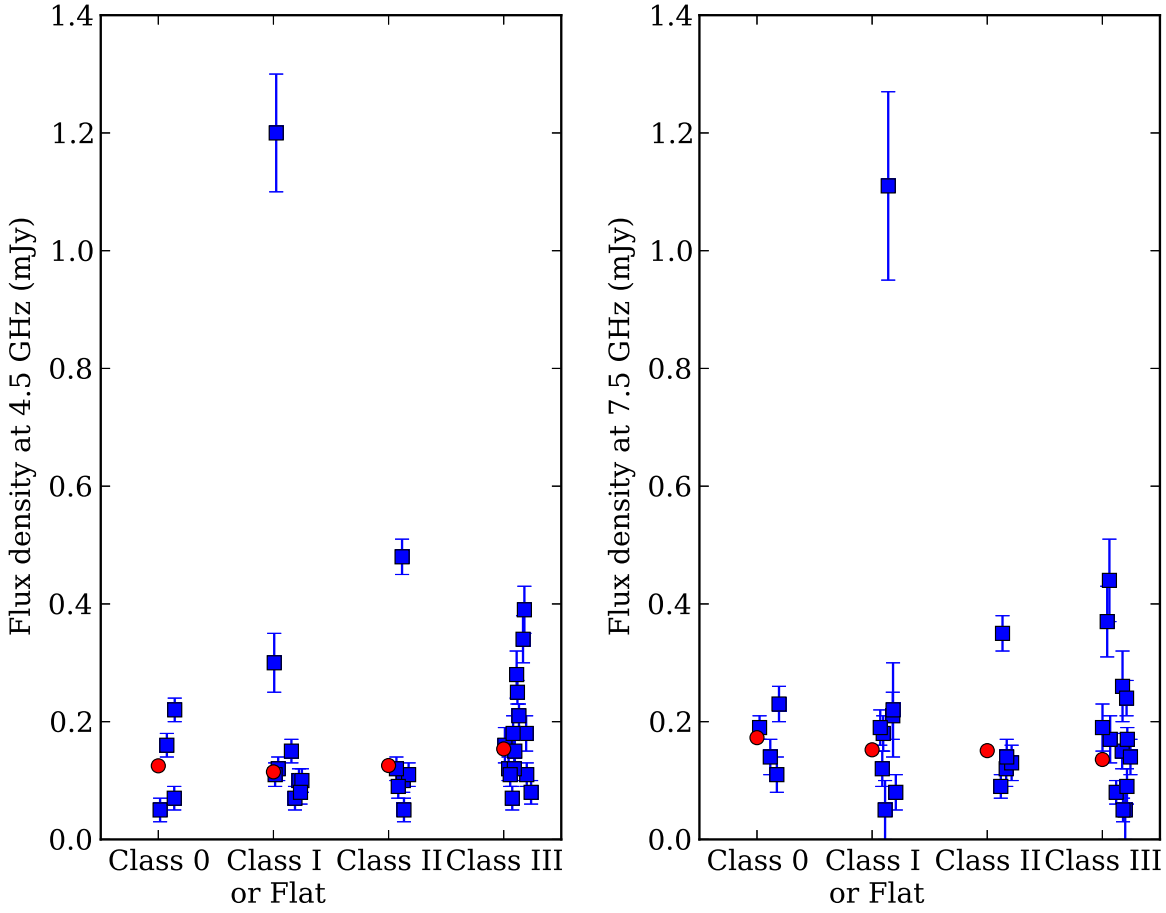

Figure 5. Radio flux at 4.5 GHz (left) and 7.5 GHz (right) as a function of YSO evolutionary status. The individual sources are shown with their error bars, and the red circles indicate the weighted average flux for each category.

coverage at uniform sensitivity) and on the observations at 4.5 GHz, which are more appropiate than those at 7.5 GHz for extragalactic objects, since those usually have negative spectral indices.

As we said before, we considered the minimum flux for a new detection to be 5σ. Assuming a uniform noise of 16 μJy, the minimum flux of the detected sources is about 80 μJy, so in the approximately 432 arcmin^2 covered by our NGC 1333 observations the number of expected background souces is 57 ± 7. In the 800 arcmin^2 covered by our IC 348 observations, the number of expected background sources is 105 ± 12. In NGC 1333, there are eight sources classified as extragalactic and eight unclassified sources previously reported at radio/X-ray wavelengths (see Table 5). In addition, there are 34 new (and unclassified) sources in this region. This suggests that all unidentified sources are background objects, since we would then have 50 background objects, compared with the expected 57 ± 7. In IC 348, there are no identified extragalactic sources, 13 unclassified radio/X-ray sources, 2 submillimeter sources (see Table 6), and 40 new (and unclassified) radio sources. This adds up to 55 sources anticipated to be background objects and remains significantly smaller than the expected 105 ± 12 background objects in the area covered by our observations. We note, however, that 18 of our radio sources are associated with objects formally classified as stars. Many of these sources come from infrared observations (Mainzer & McLean 2003; Preibisch et al. 2003) and have only been detected once. Their classification as stars is therefore somewhat uncertain. An example of this is GBS-VLA J034421.76+320918.3, as we shall see in Section 4.4.1.

For the seven individual fields a different approach is needed, because the sensitivity is not uniform across the field. We follow Anglada et al. (1998), who showed that the number of expected background sources inside a field of diameter θ_F can be expressed as

$$N = 1.4\left\{1 - \exp\left[-0.0066\left(\frac{\theta_F}{\text{arcmin}}\right)^2\left(\frac{\nu}{5\ \text{GHz}}\right)^2\right]\right\} \times \left(\frac{S_0}{\text{mJy}}\right)^{-0.75}\left(\frac{\nu}{5\ \text{GHz}}\right)^{-2.52}$$

where S_0 is the detectable flux density threshold. For the observations at 4.5 GHz the field size is $\theta_F = 15'$ and the previous expression can be written as

$$N = 1.28 S_0^{-0.75}.$$

In our observations S_0 is of order of 0.140 mJy, so we expect to detect $N = 39 \pm 6$ background sources in the seven fields observed. We find 19 unclassified radio or infrared sources and 20 new (and unclassified) radio sources in our observations of these fields. This suggests that all radio sources in these fields are extragalactic.

Combining those three cases, we expect 201 ± 14 background sources in our observations. In comparison, there are a

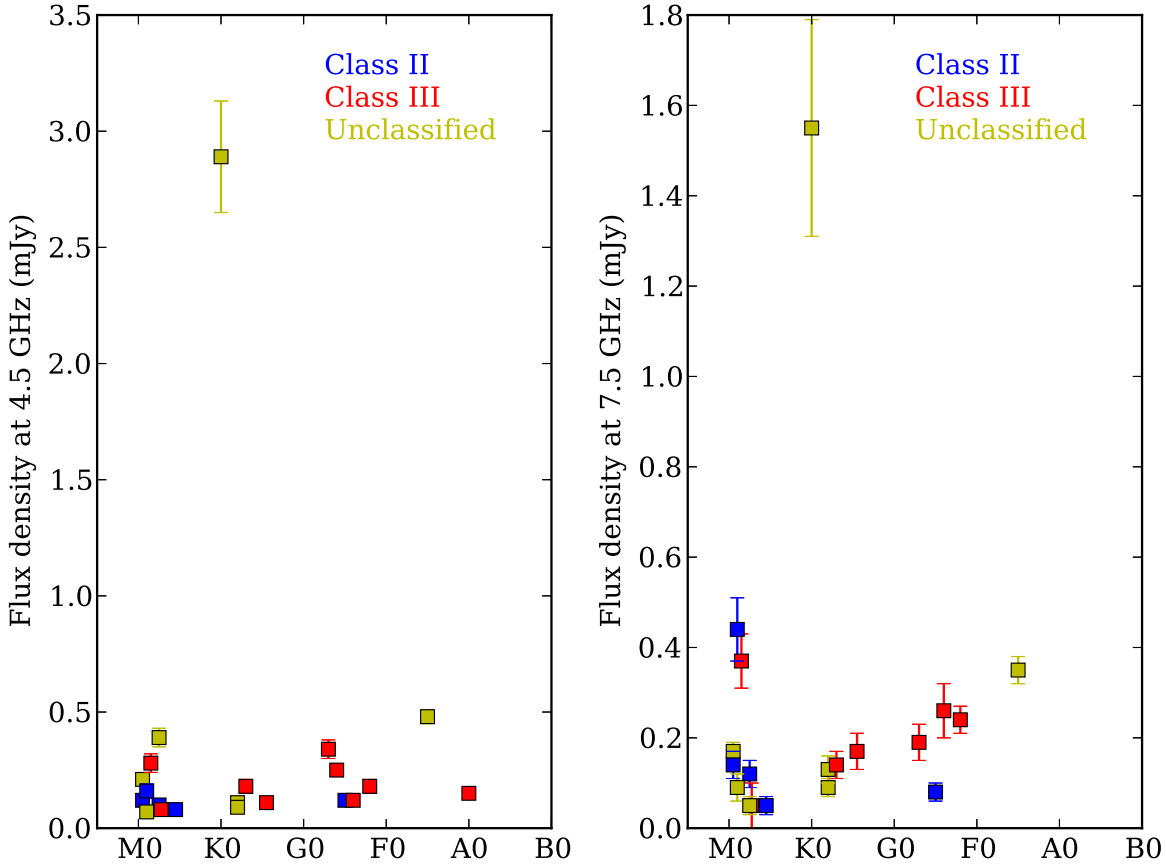

Figure 6. Radio flux at 4.5 GHz (left) and 7.5 GHz (right) as a function of YSO spectral type. Colors indicate the evolutionary class of the object as listed at the top right of the diagrams.

total of 94 new and unclassified radio sources in our observations, 8 extragalactic sources, and 42 (presumably extragalactic) radio/X-ray/IR/submillimeter sources. This adds up to 144 sources, suggesting a slight deficit, mostly corresponding to the IC 348 region, and which might be in part explained by the misclassification of some galaxies as stars (Section 4.4.1).

As discussed in Dzib et al. (2015), extragalactic radio sources tend to show little variability and to have negative spectral indices. We use these characteristics to search for possible YSO candidates among the 156 radio objects detected here that are not classified as YSOs or as extragalactic. We find that 20 objects in that sample are highly variable. These sources are listed in Table 10 and could be considered as previously unidentified YSO candidates, although, given the inherent uncertainties on the radio properties of different classes of active galactic nuclei, they could also be extragalactic sources.

4.3. The Radio–X-Ray Relation

Güdel & Benz (1993) and Benz & Güdel (1994) showed that the radio and X-ray emissions of magnetically active stars are correlated by a relation of the form

$$\frac{L_{\rm X}}{L_{\rm R}} = \kappa \cdot 10^{15.5\pm1}\ [\rm Hz].$$

From the 42 young stars in our sample, 22 have known X-ray luminosities and will be used to study the $L_{\rm X}/L_{\rm R}$ relation for YSOs. X-ray luminosities were searched in NASA's High Energy Astrophysics Science Archive Research Center (HEASARC) and have been corrected to adopt a distance of 235 pc to the entire Perseus molecular cloud (Hirota et al. 2008). In Figure 7, we plot the X-ray luminosities of the YSOs as a function of their radio luminosities at both frequencies observed in this work (magenta symbols). For comparison, we also plot the results obtained in Ophiuchus (green symbols; from Dzib et al. 2013), Serpens-W40 (red symbols; from Ortiz-León et al. 2015), Orion (yellow symbols; from Kounkel et al. 2014), and Taurus–Auriga (blue symbols; from Dzib et al. 2015). We find that for our sample $L_{\rm X}/L_{\rm R} \leqslant 10^{15.5}$, in agreement with results in other regions and also with those obtained by Gagné et al. (2004) and Forbrich et al. (2010). A relation $L_{\rm X}/L_{\rm R} \approx 10^{14\pm1}$ provides a good match to the distribution of points in this plot and is consistent with previous results of the Gould's Belt VLA Survey. The correlation, however, is not very strong (r ~0.55). This is equivalent, in terms of the Güdel–Benz relation, to $\kappa = 0.03$ for YSOs.

4.4. Comments on Individual Sources

4.4.1. Extended Sources

In our observations, we find five sources with extended emission features, one in NGC 1333 and four in IC 348.

In Figure 8 we show radio maps of source GBS-VLA J032920.67+311549.5 in NGC 1333 at 4.5 and 7.5 GHz, corresponding to the concatenation of the three epochs. This source is 0.″33 from the previously cataloged radio source VLA 32, which was classified as extragalactic (Rodríguez et al.

Table 6
Radio Sources with Known Counterparts in IC 348

GBS-VLA Name	Other Names	X-Ray[a]	Infrared[b]			Radio[c]	Object Type[d]
			SST	2M	*WISE*		
J034331.68+321451.9	⋯	⋯	⋯	⋯	⋯	NVSS 034331+321451	Rad
J034337.86+320649.2	JCMTSF J034337.8+320644	⋯	⋯	⋯	⋯	⋯	SMM
J034341.27+315754.1	JMCTSE J034341.5+315753	⋯	⋯	⋯	⋯	⋯	SMM
J034351.23+321309.1	2MASS J03435123+3213091	CXOPZ 3	Y	Y	Y	⋯	YSO
J034355.41+321008.7	2MASS J03435519+3210067	⋯	Y	Y	Y	⋯	*
J034356.01+320928.4	PSZ2003 J034356.0+320928	⋯	⋯	⋯	⋯	⋯	*
J034356.39+321042.6	PSZ2003 J034356.7+321039	⋯	⋯	⋯	⋯	⋯	*
J034357.60+320137.3	2MASS J03435759+3201373	CXOU J034357.6+320137	Y	Y	Y	FOW2011 3	YSO
J034359.65+320153.9	2MASS J03435964+3201539	CXOU J034359.6+320154	Y	Y	Y	FOW2011 4	YSO
J034401.19+321230.4	PSZ2003 J034401.2+321230	⋯	⋯	⋯	⋯	⋯	*
J034406.38+321409.8	PSZ2003 J034406.4+321410	⋯	⋯	⋯	⋯	⋯	*
J034406.65+321236.9	⋯	⋯	⋯	⋯	⋯	NVSS 034406+321235	Rad
J034408.85+320614.1	PSZ2003 J034409.2+320613	⋯	⋯	⋯	⋯	⋯	*
J034411.14+320314.0	PSZ2003 J034411.0+320315	⋯	⋯	⋯	⋯	⋯	*
J034416.17+321345.5	PSZ2003 J034416.2+321345	⋯	⋯	⋯	⋯	⋯	*
J034416.78+320956.4	2MASS J03441642+3209552	CXOPZ 32	Y	Y	Y	⋯	YSO
J034420.37+320158.4	⋯	CXOPZ 45	⋯	⋯	⋯	FOW2011 6	YSO
J034421.56+321017.4	2MASS J03442155+3210174	CXOPZ 49	Y	Y	Y	⋯	YSO
J034421.67+320624.8	2MASS J03442166+3206248	CXOPZ 52	Y	Y	Y	⋯	YSO
J034421.76+320918.3	Cl*IC 348 MM 42	⋯	⋯	⋯	⋯	NVSS 034421+320918	*
J034424.57+320357.5	2MASS J03442457+3203571	CXOPZ 64	Y	Y	Y	⋯	YSO
J034426.15+320113.1	⋯	CXOU J034426.1+320113	⋯	⋯	⋯	⋯	X
J034427.03+320443.5	2MASS J03442702+3204436	CXOPZ 77	Y	Y	Y	⋯	YSO
J034431.49+320039.6	⋯	⋯	⋯	⋯	⋯	FOW2011 7	Rad
J034431.68+321451.9	PSZ2003 J034431.6+321454	⋯	⋯	⋯	⋯	⋯	*
J034432.60+320842.4	2MASS J03443259+3208424	CXOPZ 106	Y	Y	Y	⋯	YSO
J034432.77+320837.6	2MASS J03443274+3208374	CXOPZ 108	Y	Y	Y	⋯	YSO
J034432.91+321306.6	⋯	⋯	⋯	⋯	⋯	NVSS 034433+321255	Rad
J034433.04+321241.3	⋯	CXOPZ 110	⋯	⋯	⋯	NVSS 034433+321255	X,Rad
J034433.65+321306.4	⋯	⋯	⋯	⋯	⋯	NVSS 034433+321255	Rad
J034433.91+321307.5	⋯	⋯	⋯	⋯	⋯	NVSS 034433+321255	Rad
J034434.87+320633.5	2MASS J03443487+3206337	CXOPZ 119	Y	Y	Y	⋯	YSO
J034435.89+320858.7	Cl*IC 348 MM 149	⋯	⋯	⋯	⋯	⋯	*
J034436.47+320313.4	PSZ2003 J034436.5+320317	⋯	⋯	⋯	⋯	⋯	*
J034436.92+320123.1	⋯	CXOPZ 134	⋯	⋯	⋯	⋯	Rad
J034436.93+320645.4	2MASS J03443694+3206453	CXOPZ 133	Y	Y	Y	⋯	YSO
J034438.72+320841.9	2MASS J03443871+3208420	CXOPZ 149	Y	Y	Y	⋯	YSO
J034439.17+320918.4	2MASS J03443916+3209182	CXOPZ 151	Y	Y	Y	⋯	YSO
J034443.98+320135.2	2MASS J03444389+3201373	⋯	Y	Y	⋯	⋯	YSO
J034446.82+320446.5	PSZ2003 J034446.8+320446	⋯	⋯	⋯	⋯	⋯	*
J034446.97+321455.6	⋯	⋯	⋯	⋯	⋯	NVSS 034447+321455	Rad
J034447.02+321457.9	⋯	⋯	⋯	⋯	⋯	NVSS 034447+321455	Rad
J034450.64+321906.3	2MASS J03445064+3219067	CXOPZ 187	Y	Y	Y	⋯	YSO
J034452.97+320507.5	PSZ2003 J034453.0+320507	⋯	⋯	⋯	⋯	⋯	*
J034453.84+320436.0	PSZ2003 J034453.9+320436	⋯	⋯	⋯	⋯	⋯	*
J034458.57+320715.1	PSZ2003 J034458.6+320710	⋯	⋯	⋯	⋯	⋯	*
J034507.74+320027.1	2MASS J03450773+3200272	XMMU J034507.6+320027	⋯	⋯	⋯	⋯	*
J034507.97+320401.6	Cl*IC 348 LRL 11	CXOPZ 209	Y	Y	Y	⋯	YSO
J034510.90+320822.0	⋯	CXOPZ 213	⋯	⋯	⋯	⋯	X
J034516.04+320513.9	2MASS J03451604+3205140	⋯	Y	Y	Y	⋯	*
J034532.53+320636.9	⋯	⋯	⋯	⋯	⋯	NVSS 034532+320635	Rad

Notes.
[a] CXOPZ—Preibisch & Zinnecker (2001); CXOU—*Chandra X-ray Observatory*, Unregistered; XMMU—Lumb et al. (2001), Barcons et al. (2002).
[b] *SST*—Gutermuth et al. (2009); 2M—Cutri et al. (2003); *WISE*—Cutri et al. (2012).
[c] FOW2011—Forbrich et al. (2011); NVSS—Condon et al. (1998).
[d] Object type: Rad—radio source; SMM—submillimeter source; X—X-ray source; YSO—young stellar object; *—star. Objects are marked as peculiar emitters (Rad, X-ray, IR, or smm) when information is not sufficient to determine the nature of the object.

1999; Forbrich et al. 2011). Based on the angular separation from GBS-VLA J032920.67+311549.5, it is likely that VLA 32 is the counterpart of our detection. This source is also associated with NVSS 032920+311549 reported by Condon et al. (1998) (the angular separation is only 1.″47), which has a flux at 1.4 GHz of 8.7 mJy.

All four extended sources in IC 348 are located within a square area of about 5′ × 5′ approximately centered at R.A.

Table 7
Radio Sources with Known Counterparts in Perseus Singles Fields

GBS-VLA Name	Other Names	X-Ray[a]	Infrared[b]			Radio[c]	Object Type[d]
			SST	2M	*WISE*		
J032528.40+311109.2	WISE J032528.42+311109.7	⋯	⋯	⋯	Y	NVSS 032528+311112	IR, Rad
J032827.62+304909.4	⋯	⋯	⋯	⋯	⋯	NVSS 032826+304914	Rad
J032836.79+305017.9	WISE J032836.77+305017.9	⋯	⋯	⋯	Y	⋯	IR
J032838.21+304007.9	WISE J032838.22+304008.0	⋯	⋯	⋯	Y	⋯	IR
J032840.88+304948.3	⋯	⋯	⋯	⋯	⋯	NVSS J032840+304954	Rad
J032841.15+304945.2	⋯	⋯	⋯	⋯	⋯	NVSS 032840+304954	Rad
J032852.32+304216.8	WISE J032852.32+304217.2	⋯	⋯	⋯	Y	NVSS 032852+304221	IR,Rad
J032855.81+304719.7	⋯	⋯	⋯	⋯	⋯	NVSS 032855+304720	Rad
J032906.33+304332.7	WISE J032906.29+304333.0	⋯	⋯	⋯	Y	⋯	IR
J032912.84+304558.5	WISE J032912.81+304558.6	⋯	⋯	⋯	Y	⋯	IR
J032917.16+304329.7	⋯	⋯	⋯	⋯	⋯	NVSS 032917+304432	Rad
J033100.54+313405.7	WISE J033100.51+313405.7	⋯	⋯	⋯	Y	⋯	IR
J033111.09+313904.7	WISE J033111.07+313904.9	⋯	⋯	⋯	Y	NVSS 033111+313916	IR, Rad
J033501.24+320059.9	V* IX Per	1RXS J033501.2+320104	⋯	⋯	⋯	⋯	*
J033508.31+315803.3	WISE J033508.32+315803.1	⋯	⋯	⋯	Y	⋯	IR
J033509.29+315802.5	WISE J033509.30+315803.0	⋯	⋯	⋯	Y	⋯	IR
J034300.22+293317.1	⋯	⋯	⋯	⋯	⋯	NVSS 034300+293318	Rad
J034300.32+293320.4	⋯	⋯	⋯	⋯	⋯	NVSS 034300+293318	Rad
J034307.27+293235.0	WISE J034307.29+293235.7	⋯	⋯	⋯	Y	⋯	IR
J034331.61+293534.5	2MASS J03433201+2935326	⋯	⋯	Y	⋯	⋯	*
J034356.20+293620.3	WISE J034356.20+293620.0	⋯	⋯	⋯	Y	⋯	IR

Notes.
[a] 1RXS—Voges et al. (2000), Voges et al. (1999).
[b] *SST*—Gutermuth et al. (2009); 2M—Cutri et al. (2003); *WISE*—Cutri et al. (2012).
[c] NVSS—Condon et al. (1998).
[d] Object type: *—star; IR—infrared source; Rad—radio source. Objects are marked as peculiar emitters (Rad, X-ray, IR or smm) when information is not sufficient to determine the nature of the object.

Table 8
YSOs with Polarized Emission

GBS-VLA NAME	F_V/F[a] at 4.5 GHz (%)	$\sigma_{(F_V/F)}$ at 4.5 GHz (%)	F_V/F at 7.5 GHz (%)	$\sigma_{(F_V/F)}$ at 7.5 GHz (%)	Var[b]
J032850.72+312225.2	7.3	0.9	6.3	1.3	N
J032922.29+311354.2	37.0	4.7	⋯	⋯	N
J034434.87+320633.5	69.6	14.5	⋯	⋯	N
J034450.64+321906.3	34.0	7.4	72.6	22.2	Y

Notes.
[a] F—integrated flux density in the Stokes I images; F_V—integrated flux density in the Stokes V images.
[b] Var.—Y when the source variability is higher than 50% in at least one frequency, N when it is lower.

$03^h44^m23^s$, decl. $+32°\ 11'\ 13''$. In Figures 9 and 10 we show radio maps of the region containing all these sources, corresponding to the concatenation of the three epochs. The source GBS-VLA J034411.69+321039.4 has no previously reported counterpart in the SIMBAD catalog, and no associated source was found in the NVSS catalog. The source GBS-VLA J034421.76+320918.3 is 1.″58 from previously cataloged source Cl*IC 348 MM 42 detected by Mainzer & McLean (2003) in infrared observations of IC 348. The source Cl*IC 348 MM 42 is classified as a star, yet no spectral type or spectral energy distribution (SED) classification is given for this source (Mainzer & McLean 2003; Preibisch et al. 2003). To our knowledge, there is no other identification for Cl*IC 348 MM 42. Based on their angular separation, it is likely that Cl*IC 348 MM 42 is the infrared counterpart of our detection, but if GBS-VLA J034421.76+320918.3 is actually a radio galaxy (as we will discuss later), these sources might be completely unrelated and just in the same direction as observed from the Earth. Alternatively, Cl*IC 348 MM 42 may have been erroneously identified as a star, being instead an extragalactic source. This source is also 0.″34 from radio source NVSS 034421+320918, which is reported to have an integrated flux at 1.4 GHz of 46.2 mJy (Condon et al. 1998).

The source GBS-VLA J034433.04+321241.3 is 0.″52 from previously cataloged source CXOPZ 110 detected by Preibisch & Zinnecker (2001) in *Chandra* observations. To our knowledge, no optical or infrared counterpart has been detected for CXOPZ 110. Based on its angular separation from GBS-VLA J034433.04+321241.3, we can assume CXOPZ 110 to be the counterpart of our detection. This source is also 14.″9 from radio source NVSS 034433+321255 (Condon et al. 1998).

Table 9
Young Stellar Objects Detected

GBS-VLA NAME	Spectral Type	SED[a] Clasification	Var[b]	α[b]	X-Ray	VLBI[c] Candidates	References
			NGC 1333				
J032837.10+311330.7	⋯	Class I	N	⋯	N	N	(1)
J032850.72+312225.2	⋯	⋯	N	F	N	Y	(2)
J032856.92+311622.2	M2.5	Class II	N	P	N	N	(3)
J032857.36+311415.8	⋯	Class I	N	P	N	N	(1)
J032859.25+312033.0	⋯	Flat	N	F	N	N	(4)
J032859.27+311548.2	K2.0	Class II	Y	N	Y	N	(3), (5)
J032900.37+312045.4	M4.5	⋯	Y	N	Y	N	(3)
J032901.21+312026.0	⋯	⋯	N	N	N	N	(2)
J032901.63+312018.6	⋯	Class I	N	N	N	N	(1)
J032901.96+311538.0	⋯	⋯	N	F	N	N	(2)
J032903.38+311601.6	⋯	⋯	Y	N	N	N	(2)
J032903.75+311603.7	⋯	Class II	Y	P	N	N	(5), (6)
J032904.06+311446.2	⋯	Class I	N	N	N	N	(2), (5)
J032904.26+311609.0	⋯	⋯	Y	N	N	N	(2)
J032907.75+312157.1	⋯	Class I	N	P	Y	N	(1)
J032909.14+312144.0	⋯	Class III	Y	P	Y	N	(3)
J032910.22+312335.1	⋯	Class II	N	F	N	N	(5)
J032910.39+312159.0	F5	Class II	N	N	Y	Y	(5), (9)
J032910.42+311332.0	⋯	Class 0	N	P	N	N	(1)
J032910.53+311330.9	⋯	Class 0	N	F	N	N	(1)
J032911.25+311831.1	⋯	Class 0	N	P	N	N	(1)
J032916.59+311648.7	⋯	⋯	Y	P	N	N	(2)
J032917.67+312244.9	K2/3IIIe	Class II	N	P	Y	N	(3), (6)
J032922.29+311354.2	⋯	Class I	N	N	N	Y	(5)
			IC 348				
J034351.23+321309.1	G5	Class III	Y	N	Y	N	(7), (10)
J034357.60+320137.3	M0.5	Class III	Y	N	Y	Y	(7), (10)
J034359.65+320153.9	M0.5	Class II	Y	P	Y	N	(5), (7)
J034416.78+320956.4	K0	⋯	N	N	Y	Y	(7)
J034420.37+320158.4	⋯	Class I	N	F	Y	N	(5)
J034421.56+321017.4	M1.5	Class III	Y	P	Y	Y	(7), (10)
J034421.67+320624.8	M2.75	Class III	Y	⋯	Y	N	(7), (10)
J034424.57+320357.5	M1	Class III	Y	N	Y	N	(7), (10)
J034427.03+320443.5	M1	Class III	Y	⋯	Y	N	(7), (10)
J034432.60+320842.4	M2.5	Class III	Y	F	Y	Y	(7), (10)
J034432.77+320837.6	G6	Class III	N	N	Y	N	(7), (10)
J034434.87+320633.5	K5.5	Class III	N	N	Y	N	(7), (10)
J034436.93+320645.4	G3	Class II	Y	N	Y	Y	(5), (7)
J034438.72+320841.9	K3	Class III	Y	N	Y	N	(7), (10)
J034439.17+320918.4	G8	Class III	Y	F	Y	N	(7), (10)
J034443.98+320135.2	⋯	Class 0	N	F	N	N	(1)
J034450.64+321906.3	A0	Class III	Y	F	Y	N	(7), (10)
J034507.97+320401.6	G4	Class III	Y	F	Y	Y	(7), (10)

Notes.
[a] All Class III objects corresponding to the IC 348 region are actually classified as "anemic" or "star" by Lada et al. (2006). This means that the contribution of infrared emission from the disk is very low or not existent. Based on this, we argue that this classification is equivalent to a Class III object.
[b] Var.—Y when the source variability is higher than 50% in at least one frequency, N when it is lower. α refers to the spectral index and is given as P (for positive) when it is higher than 0.2, F (for flat) when it is between –0.2 and +0.2, and N (for negative) when is is lower than –0.2. X-ray—Y when there is an X-ray flux reported in literature, N when it is not.
[c] VLBI Candidates—Sources that might have nonthermal emission and have high enough flux density to permit VLBI parallax measurements; Y when the source is a candidate, N when it is not.
References. (1) Enoch et al. 2009; (2) Rodríguez et al. 1997; Rodríguez et al. 1999; Anglada et al. 2000; (3) Winston et al. 2010; (4) Evans et al. 2009; (5) Gutermuth et al. 2009; Gutermuth et al. 2008; (6) Turnshek et al. 1980; (7) Kirk & Myers 2011; (8) Forbrich et al. 2011; (9) Connelley & Greene 2010; Connelley et al. 2008; (10) Lada et al. 2006.

The source GBS-VLA 034433.91+321307.5 has no previously reported counterpart in the SIMBAD catalog. This source is 13.″7 from radio source NVSS 034433+321255, with a reported flux at 1.4 GHz of 223.0 mJy (Condon et al. 1998). Based on the angular separation to GBS-VLA J034433.04+321241.3 and GBS-VLA 034433.91+321307.5 and the angular resolution of the NVSS observations ($\theta = 45''$), we can assume that sources GBS-VLA J034433.04+321241.3 and

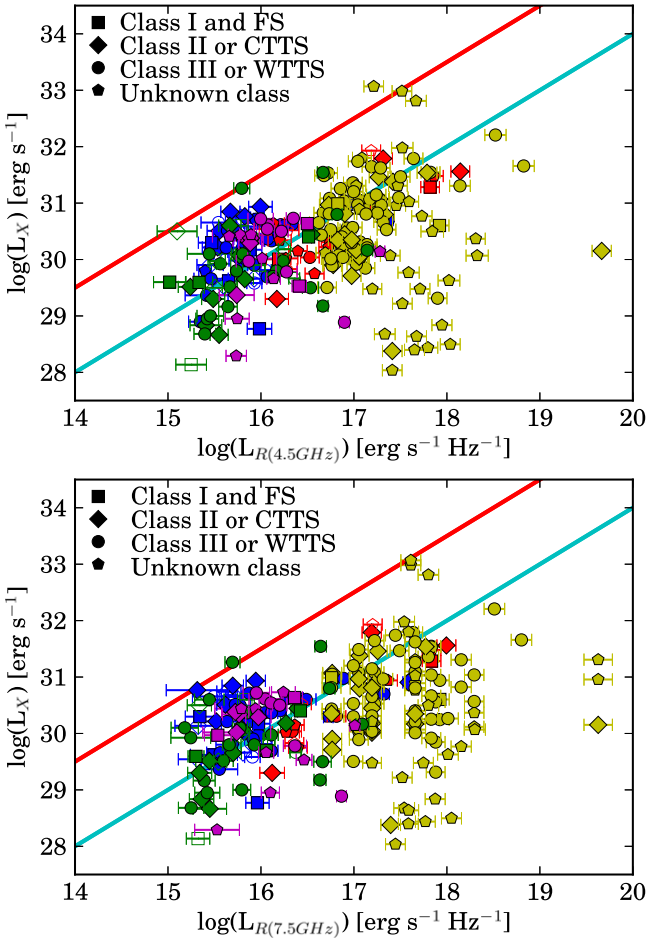

Figure 7. X-ray luminosity as a function of radio luminosity. The red line corresponds to the fiducial Güdel–Benz relation with $\kappa = 1$. The blue line corresponds to the Güdel–Benz relation but with $\kappa = 0.03$. Symbols indicate the evolutionary status of the object as explained at the top left of the diagram. Color indicates YSOs in different star-forming regions: Perseus (magenta; this work), Ophiuchus (green symbols; from Dzib et al. 2013), Serpens-W40 (red symbols; from Ortiz-León et al. 2015), Orion (yellow symbols; from Kounkel et al. 2014), and Taurus–Auriga (blue symbols; from Dzib et al. 2015). Open symbols indicate sources whose radio emission is thermal, and solid symbols indicate nonthermal radio sources.

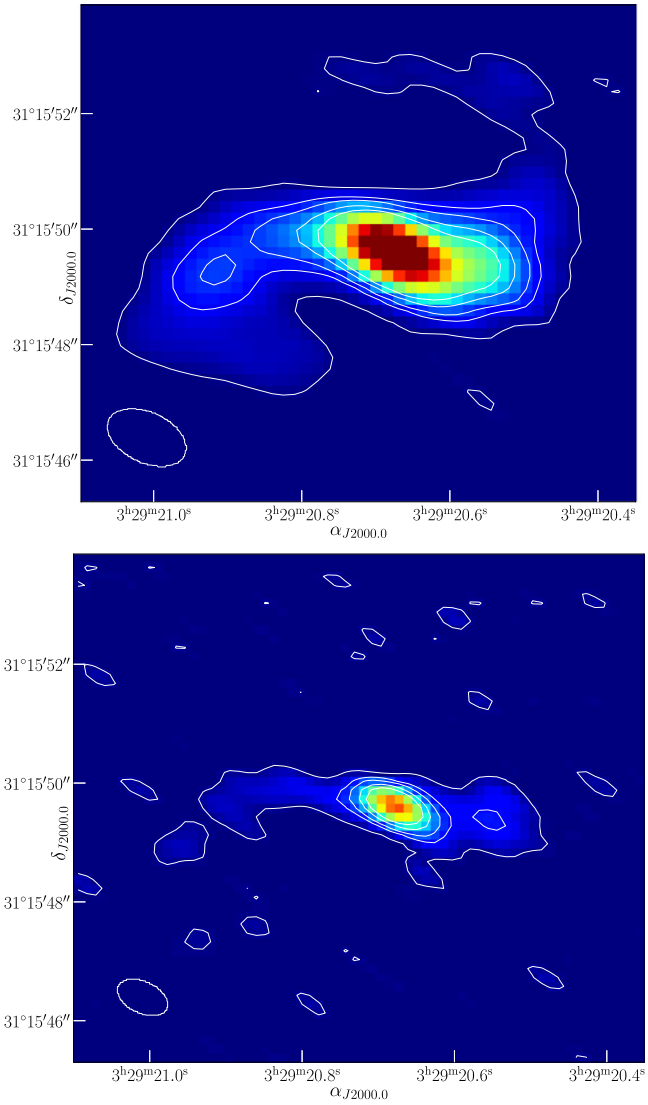

Figure 8. Top: radio map of source GBS-VLA J032920.67+311549.5 in NGC 1333 at 4.5 GHz. Contours are 2.5, 7, 10, 15, and 20 times the rms of the image (rms = 16 μJy). The synthesized beam, shown in the bottom left corner, is 1.″4 × 0.″9; P.A. = 65°. Bottom: radio map of source GBS-VLA J032920.67 +311549.5 at 7.5 GHz. Contours are 2.5, 7, 10, 15, and 20 times the rms of the image (rms = 18 μJy). The synthesized beam, shown in the bottom left corner, is 0.″9 × 0.″5; P.A. = 66°.

GBS-VLA 034433.91+321307.5 might have been detected, yet not resolved, by Condon et al. (1998) and that the NVSS 034433+321255 emission would encompass the combined emission of both of our sources. It is not completely clear from Figure 9 whether the emission feature observed directly southeast of GBS-VLA J034433.91+321307.5 can actually be associated with this source or whether it might correspond to a northeast feature of the source GBS-VLA J034433.04 +321241.3; further observations are necessary to clarify this.

As we can observe in the figures, the sources mentioned above exhibit a double and fairly symmetrical structure acompanied by some fainter, more elongated and collimated jet-like emission. All features are clearly more luminous in the 4.5 GHz map than in the 7.5 GHz map, and even brighter in the NVSS 1.4 GHz data. This is consistent with all sources having negative spectral indices, which suggests nonthermal emission, most probably synchrotron. Relativistic beaming of the synchroton emission can explain why the lobes and jet-like emission are observed stronger and more defined in one direction than the other. Based on these characteristics, we propose that these sources correspond to at least four radio galaxies. These radio galaxies are at least 10° away from the known Perseus Cluster, so we can assume that they are not members of this cluster.

4.4.2. GBS-VLA J032903.75+311603.7

In Figure 11 we show a radio map of source GBS-VLA J032903.75+311603.7. It is 0.″47 away from previously cataloged radio source VLA 4b and 0.″63 away from previously cataloged radio source VLA 4a. The sources VLA 4a and VLA 4b form a close binary separated by 0.″3 or ∼65 AU (Anglada et al. 2000, 2004). The source VLA 4b exhibits stronger millimeter emission than VLA 4a, which suggests that the source is associated with a larger amount of dust, probably a circumstellar dust disk, while the source VLA 4a appears to be the counterpart of the optically visible star SVS 13. As we can

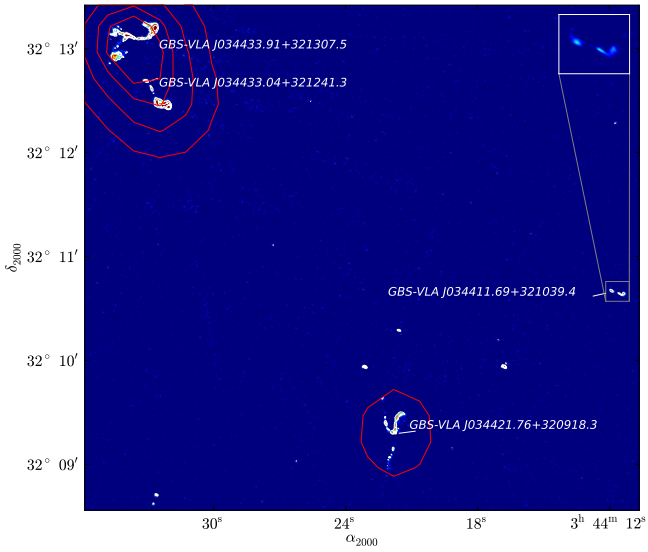

Figure 9. Radio map showing the extended sources found in IC 348 observations at 4.5 GHz overlaid with 1.4 GHz NVSS observations (red contours; Condon et al. 1998). The white contours are 4, 10, 20 and 35 times the rms of the image (rms = 16 μJy).

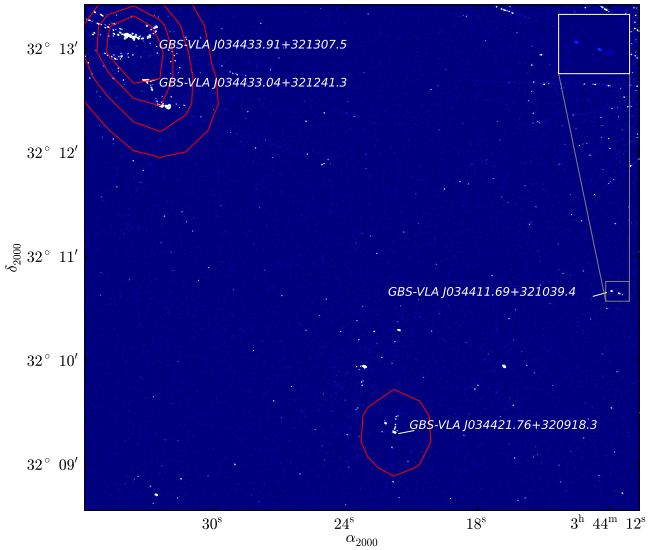

Figure 10. Radio map showing the extended sources found in IC 348 observations at 7.5 GHz overlaid with 1.4 GHz NVSS observations (red contours; Condon et al. 1998). White contours are 4, 10, 10, and 35 times the rms of the image (rms = 15 μJy).

see from the figure, we were not able to resolve the VLA 4a/4b binarity, detecting a single source instead.

4.5. Proper Motions of YSOs in Perseus

A previous and accurate analysis of proper motions for YSOs in NGC 1333 has been made by Carrasco-González et al. (2008). They used VLA data taken over 10 yr, ranging from 1989 to 1999, to measure the proper motions of four sources in NGC 1333 (VLA 2, VLA 3, VLA 4a, VLA 4b; see their Table 2 and their Figure 2). They found average values of $\mu_\alpha \cos(\delta) = 9 \pm 1$ mas yr^{-1} and $\mu_\delta = -10 \pm 2$ mas yr^{-1}. Forbrich et al. (2011) presented VLA radio observations of the NGC 1333 region obtained in 2006. In their observations they also detected and reported positions of the sources studied

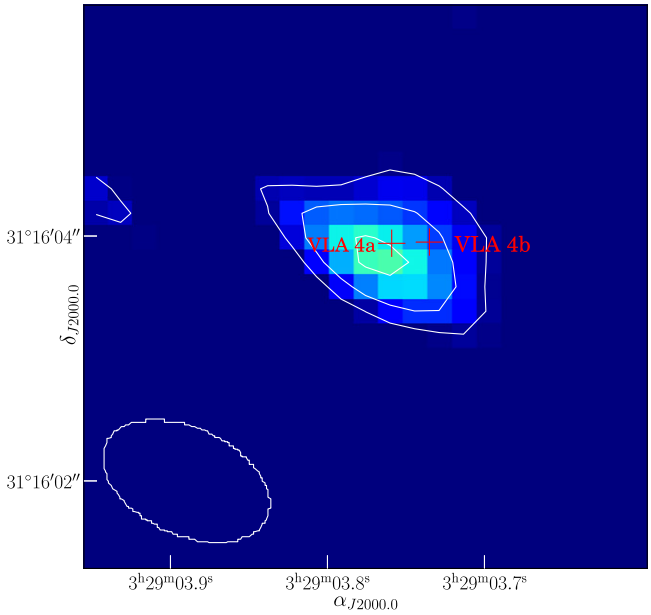

Figure 11. Radio map of source GBS-VLA J032903.75+311603.7 at 4.5 GHz. Contours are 2, 4, and 7 times the rms of the image (rms = 16 μJy). The synthesized beam, shown in the bottom left corner, is 1.″4 × 0.″9; P.A. = 65°. The red crosses indicate reported positions of VLA 4a and VLA 4b (Anglada et al. 2004).

by Carrasco-González et al. (2008) (see Tables 6 and 7 of Forbrich et al. 2011). Sources VLA 2 and VLA 3 are counterparts for our sources GBS-VLA J032901.96+311538.1 and GBS-VLA J032903.38+311601.6. We can use the position of these sources in our observations, along with the positions reported by Carrasco-González et al. (2008) and Forbrich et al. (2011), to expand the time span of the study of proper motions of these two sources. Source GBS-VLA J032903.75+311603.7 corresponds to the binary source VLA 4a/b of Carrasco-González et al. (2008), but as mentioned before, we are not able to detect this binarity. This source also appears as a single source in the Forbrich et al. (2011) observations, so it is not possible to accurately include this source in our study. Our results are shown in Figures 12 and 13. We obtain averaged values of $\mu_\alpha \cos(\delta) = 6.74 \pm 0.67$ mas yr^{-1} and $\mu_\delta = -15.32 \pm 0.92$ mas yr^{-1} (see Table 11). Our results are compatible with those reported by Carrasco-González et al. (2008) but are significantly more accurate. They might be taken as a better measure of the proper motion of the molecular cloud NGC 1333 as a whole.

5. CONCLUSIONS AND PERSPECTIVES

We have presented a multiepoch VLA survey at 4.5 and 7.5 GHz of the NGC 1333 and IC 348 clouds, along with seven individual fields in the Perseus star-forming region. The multiepoch, two-frequency strategy has enabled us to determine the radio properties of the detected sources and provided clues about the nature of their radio emission and the nature of the objects. We detected a total of 206 sources (74 in NGC 1333, 91 in IC 348, and 41 in the seven individual fields), 42 of them related to YSOs. Most of the remaining sources are probably extragalactic sources, but we provide a list of sources whose radio characteristics make them YSO candidates. There is a clear tendency for the more evolved YSOs in our sample to exhibit radio properties consistent with a nonthermal origin.

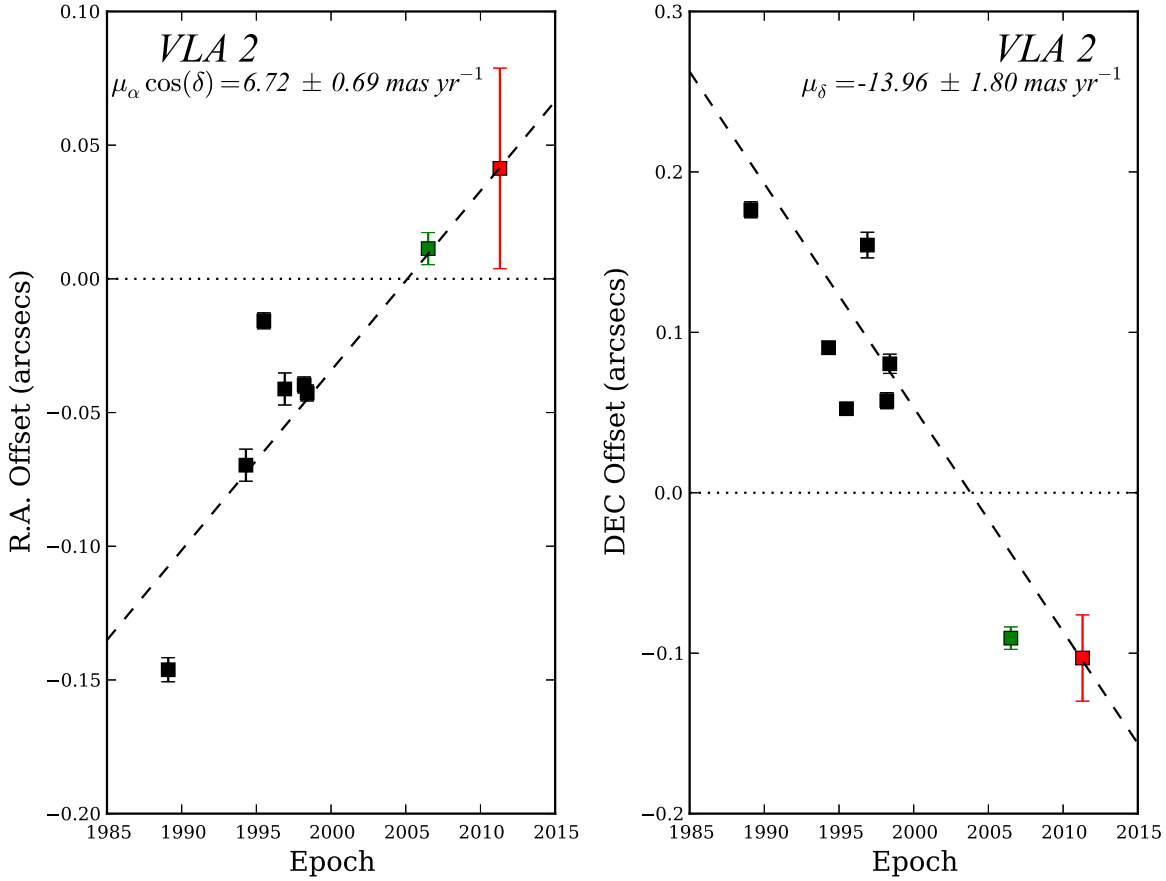

Figure 12. Position vs. time diagrams of the source GBS-VLA J032901.97+311538.1 (VLA 2). The position of the source is represented in the diagrams as R.A. and decl. offsets (in arcsec) relative to the mean position. The black squares are positions reported by Carrasco-González et al. (2008), green squares are positions reported by Forbrich et al. (2011), and red squares are positions reported in this work. The dashed line in each panel is a linear least-squares fit to the data. The values of $\mu_\alpha \cos(\delta)$ and μ_δ obtained from this fit are also labeled in each panel.

Table 10
YSO Candidates Based Only on Their Radio Properties

GBS-VLA Name	Variability$_{4.5\ \mathrm{GHz}}$ (%)	Variability$_{7.5\ \mathrm{GHz}}$ (%)	Spectral Index
	NGC 1333		
J032813.80+311755.1	>69 ± 11	…	…
J032825.98+311616.0	52 ± 11	>18 ± 35	−3.0 ± 0.5
J032846.49+312943.5	>87 ± 4	…	…
J032907.87+312348.0	>57 ± 13	>37 ± 29	−1.4 ± 1.0
J032918.56+311427.3	76 ± 15	…	…
J032933.19+312845.2	>71 ± 24	…	<−0.2 ± 0.5
J032944.99+312019.7	>58 ± 18	…	<−1.8 ± 0.4
	IC 348		
J034347.85+320555.2	>63 ± 21	…	…
J034358.35+315754.7	>66 ± 21	…	…
J034434.05+320104.3	>82 ± 14	…	…
J034437.73+321839.3	>76 ± 4	…	…
J034439.42+320128.8	>71 ± 17	…	…
J034446.97+321455.6	52 ± 7	34 ± 11	−0.9 ± 0.2
J034447.02+321457.9	43 ± 10	>61 ± 9	−1.3 ± 0.4
	Single Fields		
J032827.62+304909.4	>94 ± 2	…	…
J032841.15+304945.2	>92 ± 2	…	…
J032912.84+304558.5	>65 ± 10	…	…
J032919.25+304548.7	>96 ± 2	…	…
J033100.76+313412.3	59 ± 15	…	…
J033517.65+311650.0	50 ± 15	>28 ± 38	1.0 ± 1.2

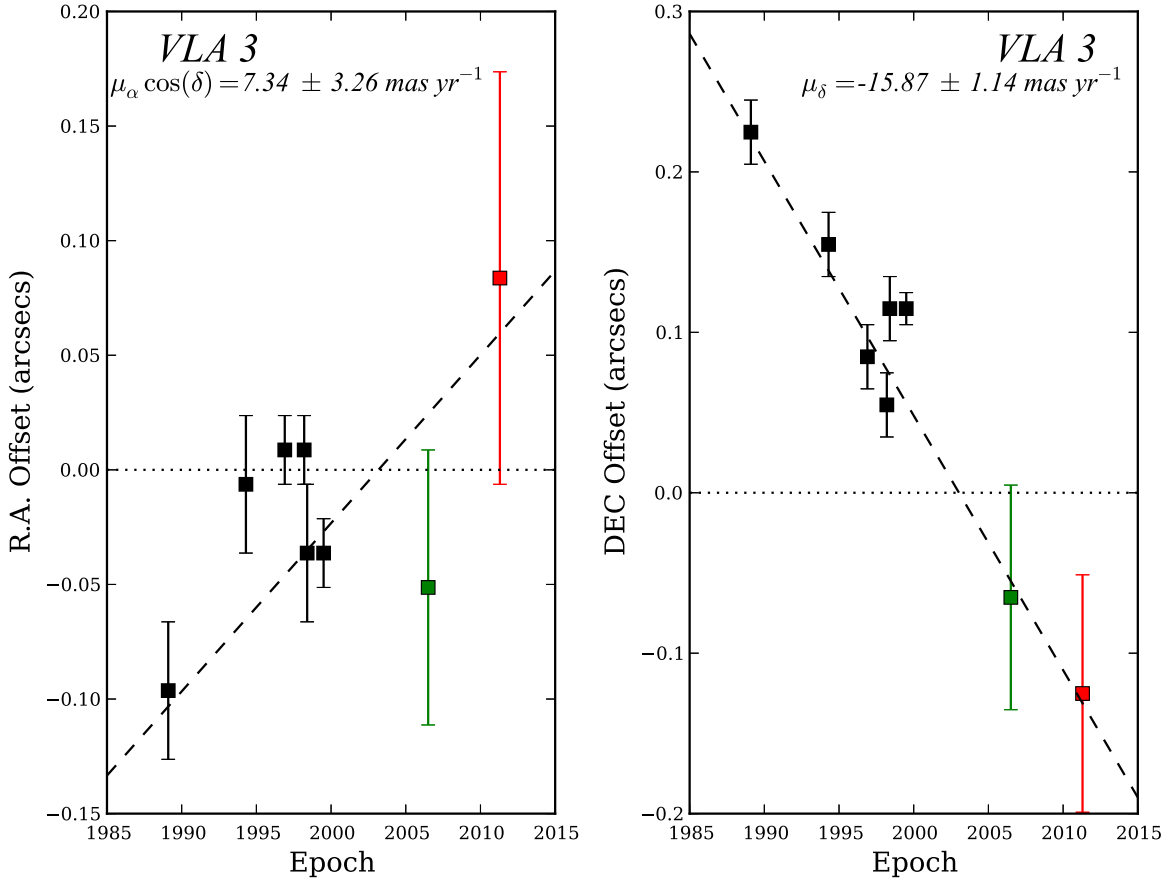

Figure 13. Position vs. time diagrams of the source GBS-VLA J032903.38+311601.7 (VLA 3). The position of the source is represented in the diagrams as R.A. and decl. offsets (in arcsec) relative to the mean position. The black squares are positions reported by Carrasco-González et al. (2008), green squares are positions reported by Forbrich et al. (2011), and red squares are positions reported in this work. The dashed line in each panel is a linear least-squares fit to the data. The values of $\mu_\alpha \cos(\delta)$ and μ_δ obtained from this fit are also labeled in each panel.

Table 11
Proper Motions of YSOs in Perseus

GBS-VLA Name	ID (lit.)	$\mu_\alpha \cos(\delta)$ (mas yr^{-1})	μ_δ (mas yr^{-1})	μ (mas yr^{-1})	v_T (km s^{-1})
GBS-VLA J032901.96+311538.1	VLA 2	6.72 ± 0.69	-13.96 ± 1.8	15 ± 2	16 ± 3
GBS-VLA J032903.38+311601.6	VLA 3	7.34 ± 3.26	-15.87 ± 1.14	17 ± 3	19 ± 3
Weighted Mean	···	6.74 ± 0.67	-15.32 ± 0.92	17 ± 2	19 ± 2

Roughly 60% of the YSOs have radio emission consistent with a nonthermal origin (gyrosynchrotron); at least nine of these sources may constitute suitable targets for future VLBI observations. By comparing our results with previous X-ray observations, we found that the sources in Perseus follow the so-called Güdel–Benz relation with $\kappa = 0.03$; this is consistent with the results in other star-forming regions.

We also detected five sources with extended emission that can clearly be associated with radio galaxies. Several of these sources had been reported in the NVSS catalog of Condon et al. (1998).

As Figure 1 shows, our observations cover only a fraction of the Perseus complex. Similar large-scale observations of other subclouds (e.g., B5, B1, L1455 or L1448) would provide a very interesting complement to the observations presented here.

G.P., L.L., L.F.R., G.N.O., J.L.R., and L.A.Z. acknowledge the financial support of DGAPA, UNAM, and CONACyT, México. The National Radio Astronomy Observatory is operated by Associated Universities, Inc., under cooperative agreement with the National Science Foundation. CASA is developed by an international consortium of scientists based at the National Radio Astronomical Observatory (NRAO), the European Southern Observatory (ESO), the National Astronomical Observatory of Japan (NAOJ), the CSIRO Australia Telescope National Facility (CSIRO/ATNF), and the Netherlands Institute for Radio Astronomy (ASTRON) under the guidance of NRAO. This research has made use of the SIMBAD database and VizieR Catalog Service, operated at CDS, Strasbourg, France.

REFERENCES

Anglada, G., Rodríguez, L. F., Osorio, M., et al. 2004, ApJL, 605, L137
Anglada, G., Rodríguez, L. F., & Torrelles, J. M. 1998, in ASP Conf. Series 132, Star Formation with the Infrared Space Observatory, ed. J. Yun & R. Liseau (San Francisco, CA: ASP), 303
Anglada, G., Rodríguez, L. F., & Torrelles, J. M. 2000, ApJL, 542, L123

Bally, J., Walawender, J., Johnstone, D., Kirk, H., & Goodman, A. 2008, in Handbook of Star Forming Regions, Vol. I, ed. B. Reipurth (San Francisco: The Northern Sky ASP Monograph Publications)
Barcons, X., Carrera, F. J., Watson, M. G., et al. 2002, A&A, 382, 522
Benz, A. O., & Güdel, M. 1994, A&A, 285, 621
Carrasco-González, C., Anglada, G., Rodríguez, L. F., Torrelles, J. M., & Osorio, M. 2008, AJ, 136, 2238
Condon, J. J., Cotton, W. D., Greisen, E. W., et al. 1998, AJ, 115, 1693
Connelley, M. S., & Greene, T. P. 2010, AJ, 140, 1214
Connelley, M. S., Reipurth, B., & Tokunaga, A. T. 2008, AJ, 135, 2496
Cutri, R. M., Skrutskie, M. F., van Dyk, S., et al. 2003, The IRSA 2MASS All-Sky Point Source Catalog, NASA/IPAC Infrared Science Archive, http://irsa.ipac.caltech.edu/applications/Gator/
Cutri, R. M., Wright, E. L., Conrow, T., et al. 2012, Explanatory Supplement to the WISE All-Sky Data Release Products, 1
Deller, A. T., Forbrich, J., & Loinard, L. 2013, A&A, 552, A51
Dzib, S., Loinard, L., Mioduszewski, A. J., et al. 2010, ApJ, 718, 610
Dzib, S. A., Loinard, L., Mioduszewski, A. J., et al. 2013, ApJ, 775, 63
Dzib, S. A., Loinard, L., Rodríguez, L. F., & Galli, P. 2014, ApJ, 788, 162
Dzib, S. A., Loinard, L., Rodríguez, L. F., et al. 2015, ApJ, 801, 91
Enoch, M. L., Evans, N. J., II, Sargent, A. I., & Glenn, J. 2009, ApJ, 692, 973
Estalella, R., Anglada, G., Rodriguez, L. F., & Garay, G. 1991, ApJ, 371, 626
Evans, N. J., II, Dunham, M. M., Jørgensen, J. K., et al. 2009, ApJS, 181, 321
Fomalont, E. B., Windhorst, R. A., Kristian, J. A., & Kellerman, K. I. 1991, AJ, 102, 1258
Forbrich, J., Massi, M., Ros, E., Brunthaler, A., & Menten, K. M. 2007, A&A, 469, 985
Forbrich, J., Osten, R. A., & Wolk, S. J. 2011, ApJ, 736, 25
Forbrich, J., Posselt, B., Covey, K. R., & Lada, C. J. 2010, ApJ, 719, 691
Gagné, M., Skinner, S. L., & Daniel, K. J. 2004, ApJ, 613, 393
Garay, G., Ramirez, S., Rodriguez, L. F., Curiel, S., & Torrelles, J. M. 1996, ApJ, 459, 193
Getman, K. V., Feigelson, E. D., Townsley, L., et al. 2002, ApJ, 575, 354
Gómez, Y., Rodríguez, L. F., & Garay, G. 2000, ApJ, 531, 861
Güdel, M., & Benz, A. O. 1993, ApJL, 405, L63
Gutermuth, R. A., Megeath, S. T., Myers, P. C., et al. 2009, ApJS, 184, 18
Gutermuth, R. A., Myers, P. C., Megeath, S. T., et al. 2008, ApJ, 674, 336
Herbst, W. 2008, in Handbook of Star Forming Regions, Vol. I, ed. B. Reipurth (San Francisco: The Northern Sky ASP Monograph Publications)
Hirota, T., Bushimata, T., Choi, Y. K., et al. 2008, PASJ, 60, 37
Hughes, V. A. 1988, ApJ, 333, 788
Hughes, V. A. 1991, ApJ, 383, 280
Hughes, V. A., Cohen, R. J., & Garrington, S. 1995, MNRAS, 272, 469
Kirk, H., & Myers, P. C. 2011, ApJ, 727, 64
Kounkel, M., Hartmann, L., Loinard, L., et al. 2014, ApJ, 790, 49
Lada, C. J., Muench, A. A., Luhman, K. L., et al. 2006, AJ, 131, 1574
Loinard, L., Mioduszewski, A. J., Torres, R. M., et al. 2011, in Revista Mexicana de Astronomía y Astrofísica Conf. Ser., ed. W. J. Henney & S. Torres-Peimbert, 40, 205
Luhman, K. L., Stauffer, J. R., Muench, A. A., et al. 2003, ApJ, 593, 1093
Lumb, D. H., Guainazzi, M., & Gondoin, P. 2001, A&A, 376, 387
Mainzer, A. K., & McLean, I. S. 2003, ApJ, 597, 555
Muench, A. A., Lada, C. J., Luhman, K. L., Muzerolle, J., & Young, E. 2007, AJ, 134, 411
Ortiz-León, G. N., Loinard, L., Mioduszewski, A. J., et al. 2015, ApJ, 805, 9
Preibisch, T. 2003, A&A, 401, 543
Preibisch, T., Stanke, T., & Zinnecker, H. 2003, A&A, 409, 147
Preibisch, T., & Zinnecker, H. 2001, AJ, 122, 866
Preibisch, T., & Zinnecker, H. 2002, AJ, 123, 1613
Rau, U., & Cornwell, T. J. 2011, A&A, 532, A71
Ridge, N. A., Di Francesco, J., Kirk, H., et al. 2006, AJ, 131, 2921
Rodriguez, L. F., Anglada, G., & Curiel, S. 1997, ApJL, 480, L125
Rodríguez, L. F., Anglada, G., & Curiel, S. 1999, ApJS, 125, 427
Simon, T. 2009, ApJ, 694, 425
Skrutskie, M. F., Cutri, R. M., Stiening, R., et al. 2006, AJ, 131, 1163
Turnshek, D. A., Turnshek, D. E., & Craine, E. R. 1980, AJ, 85, 1638
Voges, W., Aschenbach, B., Boller, T., et al. 1999, A&A, 349, 389
Voges, W., Aschenbach, B., Boller, T., et al. 2000, IAUC, 7432, 1
Walawender, J., Bally, J., Francesco, J. D., Jørgensen, J., & Getman, K. 2008, in Handbook of Star Forming Regions, Vol. I, ed. B. Reipurth (San Francisco: The Northern Sky ASP Monograph Publications)
Warin, S., Castets, A., Langer, W. D., Wilson, R. W., & Pagani, L. 1996, A&A, 306, 935
White, R. L., Becker, R. H., Helfand, D. J., & Gregg, M. D. 1997, ApJ, 475, 479
Winston, E., Megeath, S. T., Wolk, S. J., et al. 2010, AJ, 140, 266